MIPAS ozone retrieval version 8: middle atmosphere measurements

Manuel López-Puertas[1], Maya García-Comas[1], Bernd Funke[1], Thomas von Clarmann[2], Norbert Glatthor[2], Udo Grabowski[2], Sylvia Kellmann[2], Michael Kiefer[2], Alexandra Laeng[2], Andrea Linden[2], and Gabriele P. Stiller[2]

[1]Instituto de Astrofísica de Andalucía, CSIC, Granada, Spain
[2]Karlsruhe Institute of Technology, Institute of Meteorology and Climate Research, Karlsruhe, Germany

Correspondence: M. López-Puertas (puertas@iaa.es)

Abstract. We present a new version of O_3 data retrieved from the three MIPAS observations modes of the middle atmosphere (MA, UA and NLC). The O_3 profiles cover altitudes from 20 up to 100 km for daytime and up to 105 km at nighttime, for all latitudes, and the period 2005 until 2012. The data have been obtained with the IMK–IAA MIPAS level 2 data processor and are based on ESA version 8 re-calibrated radiance spectra with improved temporal stability. The processing included several improvements with respect to the previous version, such as the consistency of the microwindows and spectroscopic data with those used in the nominal mode V8R data, the O_3 a priori profiles, and updates of the non-LTE parameters and the nighttime atomic oxygen. In particular, the collisional relaxation of $O_3(v_1,v_3)$ by the atomic oxygen was reduced by a factor of two in order to obtain a better agreement of nighttime mesospheric O_3 with "non-LTE-free" measurements. Random errors are dominated by the measurement noise with 1σ values for single profiles for daytime of <5% below ~60 km, 5–10% between 60 and 70 km, 10–20% at 70–90 km and about 30% at 95 km. For nighttime, they are very similar below 70 km but smaller above (10–20% at 75–95 km, 20–30% at 95–100 km and larger than 30% above 100 km). The systematic error is ~6% below ~60 km (dominated by uncertainties in spectroscopic data), and 8–12% above ~60 km, mainly caused by non-LTE uncertainties. The systematic errors in the 80–100 km range are significantly smaller than in the previous version. The major differences with respect to the previous version are: 1) The new retrievals provide O_3 abundances in the 20–50 km altitude range larger by about 2–5% (0.2–0.5 ppmv); 2) O_3 abundances reduced by ~2–4% between 50 and 60 km in the tropics and mid-latitudes; 3) reduced O_3 abundances in the nighttime O_3 minimum just below 80 km, leading to a more realistic diurnal variation; 4) larger daytime O_3 concentrations in the secondary maximum at the tropical and mid-latitudes (~40%, 0.2–0.3 ppmv); and 5) nighttime O_3 abundances in the secondary maximum reduced by 10–30%. The O_3 profiles retrieved from the nominal mode (NOM) and the middle atmosphere modes are fully consistent in their common altitude range (20–70 km). Only at 60–70 km daytime O_3 of NOM seems to be larger than that of MA/UA by 2–10%. Compared to other satellite instruments, MIPAS seems to have a positive bias of 5–8% below 70 km. Noticeably, the new version of MIPAS data agrees much better than before with all instruments in the upper mesosphere/lower thermosphere, reducing the differences from $\sim \pm 20\%$ to $\sim \pm 10\%$. Further, the diurnal variation of O_3 in the upper mesosphere (near 80 km) has been significantly improved.

1 Introduction

Ozone is an essential variable of the atmosphere. In addition to absorbing the harmful solar UV radiation, it also plays key roles in the energy balance and chemistry of the middle and upper atmosphere (Brasseur and Solomon, 2005). Because of its importance, it has been extensively measured in the stratosphere and the mesosphere using different techniques. Kaufmann et al. (2003) and Smith et al. (2013) have provided very comprehensive reviews of O_3 observations; the former focused on those carried out before 2003, and the latter concentrated on the satellite observations performed more recently. Measurements that cover the three typical ozone maxima and, simultaneously, its diurnal variation with global latitudinal coverage are, however, scarce.

The Michelson Interferometer for Passive Atmospheric Sounding (MIPAS), a high spectral resolution limb sounder on board the Envisat satellite, measured the atmospheric O_3 from March 2002 until April 2012. The MIPAS interferometer had a spectral coverage of 4.1 to 14.7 μm (685–2410 cm^{-1}) and a very high spectral resolution. It was operated at 0.025 cm^{-1} during 2002–2004 and at 0.0625 cm^{-1} from 2005 until April 2012, and scanning the atmosphere from pole-to-pole during day (10 am) and night (10 pm) (Fischer et al., 2008). As its major objective was to understand the stratospheric chemistry and dynamics, it was observing most of the time the 6–68 km altitude range (the so-called nominal mode or 'NOM'. However, mainly after 2005, it was also regularly pointing to higher altitudes in its middle atmosphere (MA), noctilucent (NLC), and upper atmosphere (UA) measurement modes (De Laurentis, 2005; Oelhaf, 2008).

The retrieval of ozone from the NOM mode has been carried out, among others, by the Institute of Meteorology and Climate Research and Instituto de Astrofísica de Andalucía (IMK/IAA) (Glatthor et al., 2006) and the most recent retrieval version from level 1b V8.03 MIPAS spectra is described by Kiefer et al. (2023). The retrieval of O_3 from the MIPAS middle and upper atmosphere modes (including MA, UA and NLC), version V5R_O3_m22[1], has been reported by López-Puertas et al. (2018). The major difference between the retrievals of the NOM and the middle/upper atmosphere modes is the necessity of incorporating accurate non-local thermodynamic equilibrium (non-LTE) in the radiative transfer calculations for the latter.

In 2018, a new version, V8.03, of MIPAS level 1b spectra became available. This version supersedes the preceding versions. In particular, version 5, the latest used in the middle/upper atmosphere retrievals, suffered from an inadequate nonlinearity-correction of the gain calibration, that led to an artificial drift in ozone (Eckert et al., 2014; Kiefer et al., 2023). For that reason, together with the fact that this version would possibly be the last one for some time, we reprocessed the MIPAS middle and upper atmosphere O_3 data. Thus, this paper aims to document the new ozone data set, V8R_O3_m61, covering measurements recorded in the MA, UA, and NLC measurement modes. For simplicity, we refer to all three of these data sets as 'MIPAS middle atmosphere' data. They cover the period from 2005 to 2012 and the altitude ranges of 20–102 km for MA, 40–102 km for UA and 40–102 km for NLC.

The characteristics of the new level 1b V8.03 spectra are discussed in Kleinert et al. (2018) and Kiefer et al. (2021). The retrieval method of the O_3 middle atmosphere observations has been described already in Gil-López et al. (2005) and López-Puertas et al. (2018). In this version, we have also improved and updated the O_3 retrieval in several respects (see Sec. 2). Some

---

[1] 'm' is equal to 5, 6 and 7 for the MA, UA and NLC modes, respectively.

of the updates are common to the O$_3$ retrieved from the nominal mode measurements, obtained up to $\sim$70 km (Kiefer et al., 2023). Others are more specific to the MA, UA, and NLC modes, and are based mainly on the systematic differences found in the validation of V5R_O3_m22 O$_3$ data (López-Puertas et al., 2018). These updates include the O$_3$ a priori data, the revision of the non-LTE processes, and the atomic oxygen concentration during nighttime. We should note that having in mind the possible future merging of the middle atmosphere and NOM O$_3$ data, whenever possible we have maintained the same retrieval setup as in the O$_3$ NOM dataset. A comparison of the new results with the previous version V5R_O3_m22 is presented in Sec. 5, and the consistency between the NOM and MA V8R data is presented in Sec. 6.

The comparison of the middle atmosphere MIPAS O$_3$ data with respect to other satellite data (SABER, GOMOS, MLS, SMILES and ACE-FTS) has been redone, including the more recent available versions of ACE-FTS and MLS (see Sec. 7).

2 The retrieval of O$_3$ V8R_O3_m61

The MIPAS middle atmosphere V8R_O3_m61 O$_3$ retrieval is based on a constrained nonlinear least squares fitting of limb radiances. It is performed by using the IMK/IAA level 2 Scientific Processor (von Clarmann et al., 2003, 2009) supplemented with the GRANADA (Generic RAdiative traNsfer AnD non-LTE population Algorithm) algorithm (Funke et al., 2012) to account for non-LTE emissions. The different aspects of the retrieval, including the basic equations, error estimates, averaging kernels, the iteration and convergence criteria and the regularization method are described in von Clarmann et al. (2003, 2009) with recent updates in Kiefer et al. (2021, 2023). The details of the retrieval under non-LTE conditions are described by Funke et al. (2001) and the detailed non-LTE model for the O$_3$ vibrational levels in López-Puertas et al. (2018).

As mentioned above, the major motivation of this version of O$_3$ middle atmosphere data is the availability of the new level 1b radiance spectra of ESA, version 8.03, hereafter 'V8', while in the previous version, we used version V5 (5.02/5.06) of the ESA-calibrated spectra. The major changes applied to ESA V8 level 1b data are described in Kiefer et al. (2021, 2023). One of the major improvements is a better calibration introduced by a more adequate correction of the detector's non-linearities in the gain calibration. Time series of O$_3$ retrieved in the previous version V5R were shown to be affected by unrealistically large and negative drifts (Eckert et al., 2014; Hubert et al., 2020). The drifts of the ozone interim version 7, based on level 1 data that already accounted for a more adequate treatment of the gain calibration, were partially reduced but over-corrected (Laeng et al., 2018). The use of level 1b V8 spectra is expected to ameliorate this.

We recall that the MIPAS spectra used here, taken in the MA, UA, and NLC modes, cover limb tangent heights of 20–102 km at 3 km steps for MA; of 42–172 km at 3 km steps below 102 km and 5 km above, for UA; and of 39–102 km with 3-km steps in the 39–78 km and 87–102 km ranges and 1.5 km at 78–87 km for the NLC mode (De Laurentis, 2005; Oelhaf, 2008)[2]. The MIPAS horizontal field of view (FOV) is approximately 30 km and the vertical field of view is $\sim$3 km. All the measurements in the MA, UA, and NLC modes were taken at the "reduced" spectral resolution (before apodization) of 0.0625 cm^{-1}, and for clarity, we add 'R' to the level 1b version, e.g. 'V8R' and 'V5R'.

---

[2]The scan patterns and the number of measurements taken in each observing mode can be consulted at http://eodg.atm.ox.ac.uk/MIPAS/rrmodes.html and http://eodg.atm.ox.ac.uk/MIPAS/L2OXF/ (last checked 10 Sep 2023).

2.1 Retrieval updates common to the nominal and middle atmosphere measurement modes

Many of the updates applied to the ozone retrieval from the nominal-mode measurements (Kiefer et al., 2023) apply also to the
middle atmosphere retrievals presented here. For completeness, they are briefly described in this section. Those more specific
to the middle atmosphere modes (MA, UA, NLC) are described in Sec. 2.2.

2.1.1 Retrieved temperatures

Following the usual sequence of retrieval steps, the temperature and the tangent altitude information retrieved in a previous
step from V8R spectra are included in the O_3 retrieval. This version of the temperature retrieval includes, in addition to the
level 1b spectra, several updates and improvements with respect to the V5R version. Among them, the most important are:
the a priori temperature above 43 km (updated from NRLMSISE-00 to SD-WACCM4), the atomic oxygen (updated from the
NRLMSISE-00 model to the SD-WACCM4 model at MIPAS geolocations and corrected with MIPAS V5R climatology); and
the CO_2 concentration now taken from the SD-WACCM4 climatology (see, Kiefer et al., 2021; García-Comas et al., 2023, for
more details).

In nominal mode retrievals, where high-altitude temperatures depend largely on a priori assumptions, the new temperature
retrieval led to a significant improvement of polar lower mesospheric O_3 during large stratospheric warnings (Kiefer et al.,
2023). This effect, however, is small in the current MA mode O_3, because in this mode the retrieved temperature at higher
altitudes does not depend that much on a priori assumptions.

A further improvement of the preceding retrieval of temperature in V8R is the inclusion of its variability along the line-of-
sight (LOS). This was considered by including an a priori 3D field with its horizontal structure provided by a priori information
and its vertical structure scaled by the retrieved temperature (Kiefer et al., 2021). Following our sequential retrieval approach,
the resulting 3D temperature field was used in the forward calculations of O_3 limb radiances. Likewise, this temperature field
was used to correct the non-LTE populations along the LOS. In the previous O_3 version, the variations of temperature along
the LOS were implemented more approximately by retrieving a linear horizontal temperature gradient around the tangent point
(Kiefer et al., 2021).

2.1.2 Background continuum, radiance offset and water vapour interference

The IMK/IAA processor retrieves, jointly with the O_3 abundance, a background continuum radiation and a zero-level calibra-
tion offset. Both, the continuum and the offset are retrieved at each microwindow (MW) and altitude.

The uppermost altitude of the continuum retrieval has been extended from 50 to 60 km. The background continuum is
strongly constrained to zero above 60 km (we used 50 km in the previous version), and the vertical offset profiles for the
microwindows in band A (MWs #1–30) and band AB (MWs #31–38) (see Table A1) are strongly regularised towards the a
priori values taken from the empirically determined offset correction profiles by Kleinert et al. (2018). See more details in
Kiefer et al. (2023).

Further, in this version, the abundance of H_2O is also jointly retrieved with those parameters. This is done in order to avoid the propagation of uncertainties of the a priori H_2O. Note, however, that these joint-retrieved H_2O profiles are not used further because they are of sub-optimal quality since the spectral range was selected for the retrieval of ozone but not for H_2O (Kiefer et al., 2023).

2.1.3 Microwindows and spectroscopy

As for temperature and other gases, in the retrieval of O_3 we use small spectral regions (microwindows) covering ro-vibrational emissions of the main O_3 isotope. These MWs vary with tangent altitudes in order to minimise errors and optimise computation time. Glatthor et al. (2018) has shown that the O_3 spectroscopic data in MIPAS band A (685–980 cm^{-1}) and those in the AB-band (1010–1180 cm^{-1}) are inconsistent. Further, Laeng et al. (2014, 2015) found that the use of microwindows in the AB-band, instead of in band A, leads to a positive bias in MIPAS ozone profiles in the upper troposphere and lower stratosphere. Thus, whenever possible, we used MWs in band A. However, in the mesosphere and lower thermosphere, the O_3 lines in band A are too weak and the spectra are noisy; hence the use of MWs in the AB-band was necessary.

The MWs used in this version are essentially the same as in the previous version, and are listed in Table A1 for easy reference. Only minor changes were made. In particular, MW#8 (720.75–723.688 cm^{-1}) was excluded due to CO_2 line mixing, and MWs #37 and #38 near 1053 and 1055 cm^{-1} were slightly reduced to remove the radiance contribution of CO_2 laser band lines. The MWs used below 50 km are the same as those used in the NOM O_3 retrieval (all located in the A band) and those used between 50 and 70 km are very similar (both from the AB band) (Kiefer et al., 2023).

The O_3 spectroscopic data from the HITRAN 2008 database (Rothman et al., 2009) used in the previous version of the O_3 retrieval were replaced with those of the MIPAS pf3.2 database (Flaud et al., 2003a,b). This change was motivated because the MIPAS spectroscopic database has smaller inconsistencies between the line strengths in the spectral range of the MIPAS A and AB bands and because in the HITRAN dataset, there is an unrealistic large change in the air broadening coefficients near 797 cm^{-1} (Glatthor et al., 2018). For the interfering species, we used HITRAN 2016 (Gordon et al., 2017). CO_2 line-mixing coefficients have been re-calculated for the new spectroscopic data.

2.1.4 Other changes in the forward model and inputs parameters

Another less important change included in this version is the different concentrations of the interfering species. While in the previous version we used a specifically tailored climatology, here we constructed the interfering species dataset based on previous V5R version results (see Kiefer et al., 2021). The CO_2 concentration is taken from the SD-WACCM4 climatologies (see, Kiefer et al., 2021; García-Comas et al., 2023).

In the current version, we used an internal spectroscopic grid in the forward model, w_{grid}, of 0.0009765625 cm^{-1}, instead of the finer grid of 5×10^{-4} cm^{-1} used in the previous version. For convenience, w_{grid} was chosen as that which is closer to 10^{-3} cm^{-1} and fulfills that $0.0625/w_{grid} = 2^N$, where 0.0625 (cm^{-1}) is the spectral resolution before apodization and N is an integer number, $N = 6$ in our case. Tests performed show that the use of that coarser spectral grid has a negligible effect on the retrieved O_3. That is, it adequately accounts for the mesospheric O_3 Doppler line shape. In turn, it allows us to reduce the

CPU time consumed by the retrieval. On the other hand, the wider frequency range for the Norton-Beer "strong" apodization (Norton and Beer, 1976) of calculated spectra used now contributes to increase the CPU time.

2.2 Retrieval updates specific to middle atmosphere measurement modes

In this section, we describe the updates which are more relevant or exclusive to the retrieval of O_3 from the MA, UA and NLC observation modes, and hence are more relevant for the O_3 retrieved above $\sim$70 km.

2.2.1 Regularisation

The retrievals are performed from the surface to 120 km over a fixed altitude grid of 1 km up to 50 km, at 72–75 km, and at 77–88 km; of 2 km at 50–72 km, 75–77 km, and 88–102 km; and of 5 km from 105 up to 120 km. Contrary to the retrievals from the nominal observation mode (Kiefer et al., 2023), which are linear in volume mixing ratio (VMR), in the middle atmospheric measurement modes we retrieve the logarithm of VMR. Forward calculations are performed using the same grid. As this grid is finer than the MIPAS vertical sampling of 3 km (except in the NLC mode at 78–87 km where it is 1.5 km), we used a regularisation; a Tikhonov-type first order smoothing constraint in our case (Tikhonov, 1963). The regularisation used in this version has not changed since version 5.

2.2.2 A priori O_3

The a priori O_3 in the mesosphere and lower thermosphere has changed significantly and affects principally the upper mesospheric daytime O_3 mixing ratio. We recall that the Tikhonov regularization chosen does not systematically push the retrieved ozone profile towards the a priori but only constrains the shape of the vertical profile.

In the previous version we used the 2D field from Garcia and Solomon (1994) which had the O_3 daytime secondary maximum at altitudes lower than recent measurements (López-Puertas et al., 2018). Here, the O_3 a priori is essentially a MIPAS O_3 V5R zonal mean climatology (obtained from MA and UA monthly composites, 10° resolution, and linearly interpolated in between). This climatology has been modified to account for the poorer MIPAS vertical resolution in the upper mesosphere by correcting with $O_{3,corr} = O_{3,uncorr} \times [O_{3,W}/O_{3,W\_AK}]$, where $O_{3,W}$ is taken from the SD-WACCM4 climatology, the Whole Atmosphere Community Climate Model Version 4 simulations (Marsh, 2011; Marsh et al., 2013) of a specified dynamics run (Garcia et al., 2017), and O_{3,W_AK} is the same $O_{3,W}$ climatology but with the MIPAS averaging kernels applied. With this correction, the MIPAS climatology remains essentially unaltered below $\sim$70 km. Above, the overall magnitude of the MIPAS V5R ozone abundances is maintained, while unresolved profile features are incorporated from the WACCM climatology.

2.2.3 Non-LTE: collisional and reaction rates

The ozone non-LTE model used in this version is described in detail by López-Puertas et al. (2018); see Sec. 2 and Tables 1 and 2 in that work. We describe here the major changes in the model that apply to this version. First, we discuss the collisional

rates and later on, the species abundances required by the non-LTE model and not measured by MIPAS, i.e., the atomic oxygen and hydrogen concentrations.

The major uncertainty in the O_3 non-LTE model is the deactivation of $O_3(v_1, v_3)$ by atomic oxygen, either by chemical quenching, $O_3(v_1, v_3) + O \rightarrow O_2 + O_2$, or by inelastic collisions, $O_3(v_1, v_2, v_3) + O \rightarrow O_3(v_1', v_3') + O + \Delta E$, process $k_{vt,O}$ in Table 1. The uncertainty comes not only from the rates themselves but also from the uncertain amount of atomic oxygen, which is not measured but derived or constrained by the retrieved O_3 in an iterative process (López-Puertas et al., 2018; Mlynczak et al., 2013). For larger rates or larger O concentrations, the deactivation is stronger, which leads to lower populations for the emitting O_3 states and hence larger O_3 abundances.

In the validation of the previous version of O_3 we found that the nighttime upper mesospheric O_3 was larger by $\sim$20% than in most of the other instruments (López-Puertas et al., 2018). Thus, to obtain a better agreement, we reduced the relaxation of O_3 by O, $O_3(v_1, v_3) + O$, $k_{vt,O}$, by a factor of two, e.g., 4.65×10^{-12} cm^{3}s^{-1}. Note that the chemical quenching, $O_3(v_1, v_3) + O \rightarrow O_2 + O_2$, was already neglected in the previous version, as suggested by West et al. (1978). The assumed rate is within the uncertainties of the laboratory measurements but at the lower limit measured by West et al. (1976) (see the discussion in López-Puertas et al., 2018). More recently, Castle et al. (2014) have measured the thermal relaxation of the lower-energy v_2 mode[3] in collisions with O at room temperature, finding a value of $(2.2 \pm 0.5) \times 10^{-12}$ cm^{3}s^{-1}. Our selected value is still reasonable because, although still larger, it is closer to the relaxation of the lower-energy v_2 mode, whose relaxation is expected to be more efficient.

2.2.4 Trace gas concentrations relevant for non-LTE modelling

As shown above, the retrieval of O_3 mixing ratios under non-LTE conditions requires knowledge of the atomic oxygen concentration, [O]. In our retrieval, we constrain [O] by assuming that O_3 is in photochemical equilibrium with O and using the O_3 abundance retrieved in the previous iteration of the inversion (daytime) or from the previous version (nighttime). This is a reasonable approach above around 60 km during daytime and $\sim$80 km at nighttime because of the rapid timescales for ozone production and loss in this region. Below those altitudes collisions with O are negligible.

2.2.4.1 Daytime

Taking into account the major photochemical reactions affecting O_3 in the mesosphere and lower thermosphere (see Table 1), the O concentration for daytime conditions can be well approximated by

$$[O]_d = \frac{(J_{O3} + k_2[H]) \, [O_3]}{k_1 \, [O_2] \, [M] - k_3[O_3]} \approx \frac{J_{O3} \, [O_3]}{k_1 \, [O_2] \, [M] - k_3[O_3]}, \tag{1}$$

where the chemical loss of O_3 by H has been neglected. In summary, for daytime, the required [O] is computed by using this equation and the O_3 retrieved in the previous iteration.

---

[3]The 9.6 μm emission used here to retrieve O_3 in the mesosphere and lower thermosphere comes from the Δv_3 and Δv_1 bands.

Table 1. Major photochemical reactions affecting O_3 in the mesosphere and lower thermosphere and processes affecting the population of the O_3 vibrational levels.

No.	Process	Rate coefficient (cm^3s^{-1})[†]	Assumed uncertainty (%)
1	k_1: $O_2 + O + M^{\star} \rightarrow O_3(v_1,v_2,v_3) + M^{\star}$	$6.0 \times 10^{-34} (T/300)^{-2.4}$	10
2	k_2: $H + O_3 \rightarrow OH^*(v) + O_2$	$1.4 \times 10^{-10} \exp(-470/T)$	10
3	k_3: $O + O_3 \rightarrow O_2 + O_2$	$8.0 \times 10^{-12} \exp(-2060/T)$	10
4	J_{O3}: $O_3 + h\nu \rightarrow O_2 + O$	TUV version 5.3.2 (see text)	7
5	$k_{vt,M}$: $O_3(v_1,v_2,v_3) + M^{\star} \rightleftharpoons O_3(v'_1,v'_2,v'_3) + M^{\star}$	See processes 2a-2d in Table 7 of Funke et al. (2012)[‡]	20
6	$k_{vt,O}$: $O_3(v_1,v_2,v_3) + O \rightarrow O_3(v'_1,v'_2,v'_3) + O$	4.65×10^{-12}	50

[$\star$]M represents N_2 and O_2. [†]Except for k_1 that is in cm^6s^{-1}. Note that the energy of the $O_3(v_1,v_2,v_3)$ level is larger than that of $O_3(v'_1,v'_2,v'_3)$.

[‡]k_d (process 2c) is limited to a minimum value of 4×10^{-16} cm^3s^{-1} at temperatures below 200 K (López-Puertas et al., 2018).

The photo-absorption coefficient J_{O3} is calculated by using the TUV model version 5.3.2[4], which includes the MIP6 solar spectral irradiance. In the previous version, we used TUV version 4.2 which uses the less variable SUSIM (Solar Ultraviolet Spectral Irradiance Monitor) solar spectral radiance. The new J_{O3} coefficient is $\sim$10% smaller below 100 km, which leads to a daytime [O] of $\sim$10% smaller below 90 km, and is very similar near 100 km. As explained above, the effect of this change in the non-LTE model tends to decrease the retrieved O_3.

2.2.4.2 Nighttime

During nighttime, the photochemical equilibrium of O_3 leads to

$$[O]_n \approx \frac{k_2[H]\,[O_3]}{k_1\,[O_2]\,[M] - k_3\,[O_3]}. \tag{2}$$

In the previous version we calculated $[O]_n$ from Eq. (2) and taking [H] from the NRLMSIS-00 model (Picone et al., 2002). Here [H] was inferred from MIPAS daytime and nighttime O_3 measurements in the altitude range where the O vmr is free of photochemically-induced diurnal variations (above $\sim$80 km). In that region, the atomic oxygen vmr has no significant diurnal variations except those caused by tides, which we consider related by $O_{vmr,n} = O_{vmr,d} \times f_t$, where f_t is a tidal correction factor. Thus, by combining Eqs. 1 and 2, using f_t, and defining the chemical losses for daytime (10 am) $L_d = k_{1,d}\,[O_2]_d\,[M]_d - k_{3,d}\,[O_3]_d$, and nighttime (10 pm) $L_n = k_{1,n}\,[O_2]_n\,[M]_n - k_{3,n}\,[O_3]_n$, we obtain

$$[H]_n = \frac{J_{O3}}{k_{2,n}} \frac{L_n}{L_d} \frac{O_{3,vmr,d}}{O_{3,vmr,n}} f_t, \tag{3}$$

where we consider different densities and temperatures for daytime and nighttime. The tidal correction factor f_t for atomic oxygen can be constructed by making use of the pressure difference Δp between 10 am and 10 pm at a given potential temperature

[4]https://www2.acom.ucar.edu/modeling/tropospheric-ultraviolet-and-visible-tuv-radiation-model.
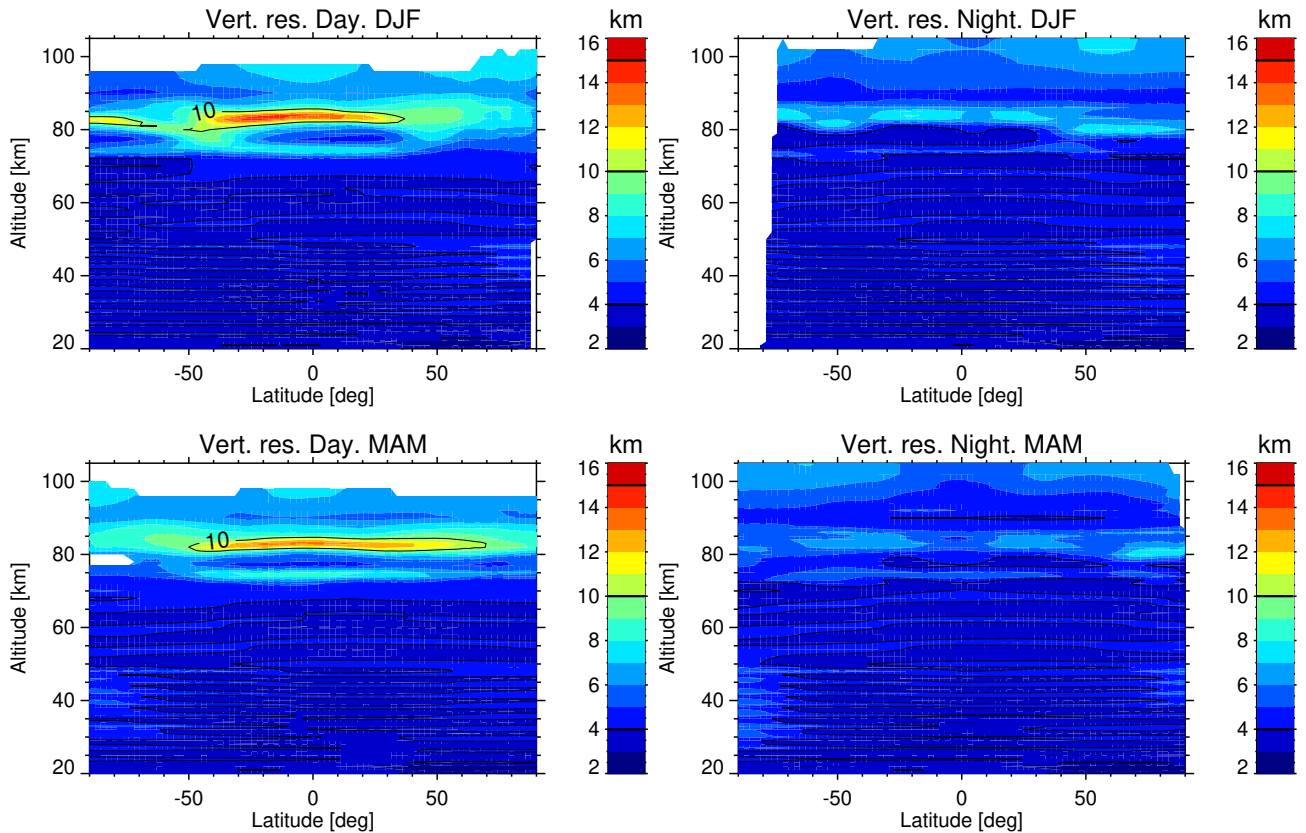
Figure 1. Latitude-altitude cross sections of MIPAS MA vertical resolution for daytime (left panels) and nighttime (right panels) conditions. The top panels are for solstice (December-January-February: DJF) and the bottom panels for equinox (March-April-May; MAM). The means include all measurements from 2005 to 2012. White areas denote regions where the retrieved O_3 is not significant. Contour lines are marked in the colour bar scale.

level by

$$f_t = 1 + \frac{O_{3,\mathrm{vmr,d}}(p - \Delta p)}{O_{3,\mathrm{vmr,d}}(p)}. \tag{4}$$

Unfortunately, MIPAS did not measure daytime and nighttime O_3 at the same geolocations. This means that information on $[H]_n$ can be obtained from MIPAS only on a climatological basis, e.g., from O_3 vmr day- and nighttime climatologies. In order to incorporate the transient variability we employ SD-WACCM4 simulations (see Sec. 2.2.2) sampled at MIPAS geolocations, $[H_W]_n(\mathrm{geo})$, e.g.,

$$[H]_n(\mathrm{geo}) = [H_W]_n(\mathrm{geo})\, f_c \tag{5}$$

where, to be consistent with the climatological MIPAS $[H]_n$, they were corrected by the climatological MIPAS to WACCM ratio

$$f_c = [H_{\mathrm{MIP}}]_n(\mathrm{month}, \mathrm{p}, \mathrm{lat}) / [H_W]_n(\mathrm{month}, \mathrm{p}, \mathrm{lat}). \tag{6}$$
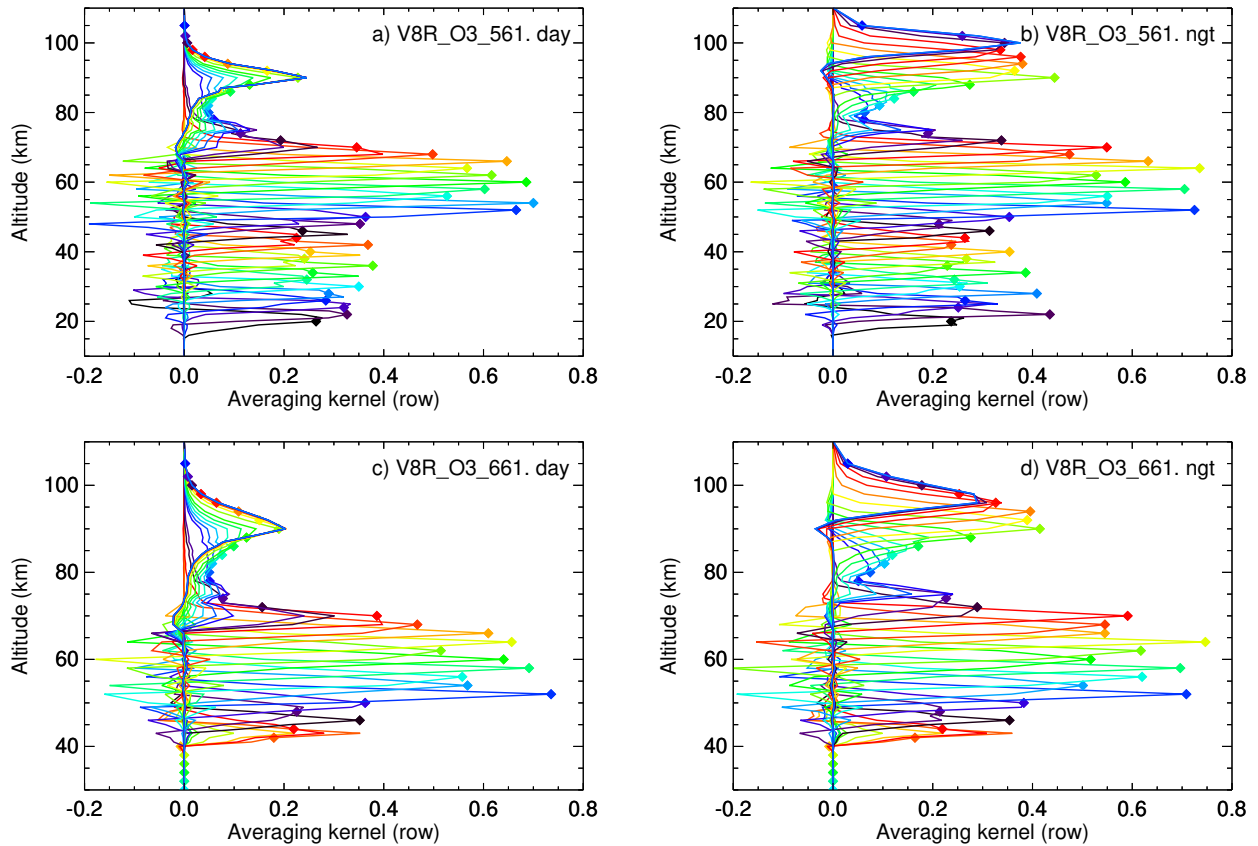
Figure 2. Rows of the averaging kernel matrix for ozone profiles recorded during the MA (top row) and UA (bottom row) measurement period. The corresponding averaging kernel diagonal elements are indicated by symbols. The left panels show the values for daytime conditions and the right panels for nighttime conditions. Kernel rows are shown every 2 km up to 102 km and at 115 km. MA data in a) are taken from 1 Sep 2009 (Envisat orbit 39234) at 49.8°N, 152.8°E, and in b) from 10 Sep 2009 (Envisat orbit 39364) at 42.0°N, 51.1°W. UA data in c) and d) are taken from 1 Sep 2009 (Envisat orbit 39235) at 49.8°N, 127.9°E, and at 40.5°N, 46.6°W, respectively.

This method for generating the a priori [H] has two caveats. First, SD-WACCM4 is free-running above the stratopause, resulting in deviations from the observed meteorology. However, larger perturbations of MLT dynamics caused by wave propagation from the lower atmosphere, which may have a noticeable impact on atomic hydrogen, are still represented reasonably well in comparison to a merely climatological a priori. Secondly, the correction factor f_c is based mainly on MIPAS V5R O_3 data. It might change if derived from the V8R reprocessed ozone data, which would then raise the necessity for iteration. To sort out this we computed f_c factors from the resulting V8R ozone data. Differences in the updated f_c are generally smaller than 15%, except in the tropics, where deviations can be as large as 30%. The nighttime [H] concentration derived from MIPAS V5R data in the 80–100 km altitude range agrees well, within a 20–25%, with the [H] from the NRLMSIS 2.0 empirical model (Emmert et al., 2021) for all latitudes and seasons, except in the tropics where the differences are within 20% and 50%, with [H] derived from MIPAS being smaller.

The atomic oxygen described above is available in the region where we retrieve O_3. Above approximately 97 km, we used the atomic oxygen from SD-WACCM4 simulations (see García-Comas et al., 2023).

Even if we tried to avoid CO_2 lines in the MW selection (see above), to be on the safe side, we also included the contribution of CO_2 lines in the forward model. The CO_2 bands are also considered in non-LTE. A detailed description of the CO_2 non-LTE model and all the required input parameters can be found in Jurado-Navarro et al. (2016).

3   Characterisation of the retrieved O_3 mixing ratios

Ozone is reliably retrieved from 20 km in the MA mode (40 km for the UA and NLC modes) up to ∼95 km during illuminated conditions and up to ∼105 km during dark conditions. Figures D1 and D2 show monthly climatologies of MIPAS V8R O_3 for daytime (10 am) and nighttime (10 pm) conditions respectively, from the mid-stratosphere up to the lower thermosphere. Their major features, including their vertical and latitude distributions and diurnal variations, are discussed in detail in López-Puertas et al. (2018). The updated figures for version V8R are shown in Appendix D.

The zonal mean of the vertical resolution for the middle atmosphere (MA) mode for solstice and equinox conditions and daytime and nighttime are shown in Figure 1. The vertical resolution of the retrieved ozone is given by the full width at half maximum of the averaging kernels rows. These are shown for four typical examples corresponding to MA and UA for day and nighttime in Figure 2. For daytime, the vertical resolution is about 3–4 km below 70 km, 6–8 km at 70–80 km, 8–10 km at 80–90 km (coarser in tropical regions), and 5–7 km at the secondary maximum (90–100 km). For nighttime conditions, the vertical resolution is similar below 70 km, but it is better in the upper mesosphere and lower thermosphere. Overall, it is about 4-6 km at 70–100 km (except a narrow region near 80 km where it takes values of 6–8 km), ∼4–5 km at the secondary maximum; and 6–8 km at 100–105 km. The vertical resolution has not changed significantly from the previous version. If anything, they are slightly better now above about 80 km, more markedly during nighttime conditions. The results for the UA and NLC modes are very similar in the common retrieved region.

The criteria recommended for using the data are the same as in the previous version, which we recall here. First, the individual values of the retrieved profiles where the diagonal value (or the mean diagonal value when averaging) of the averaging kernel is

less (in absolute value) than 0.03 should not be used (data with smaller values are considered non-trustworthy); and, secondly, the values corresponding to altitudes not sounded by MIPAS, which are flagged by the visibility flag, should not be used.
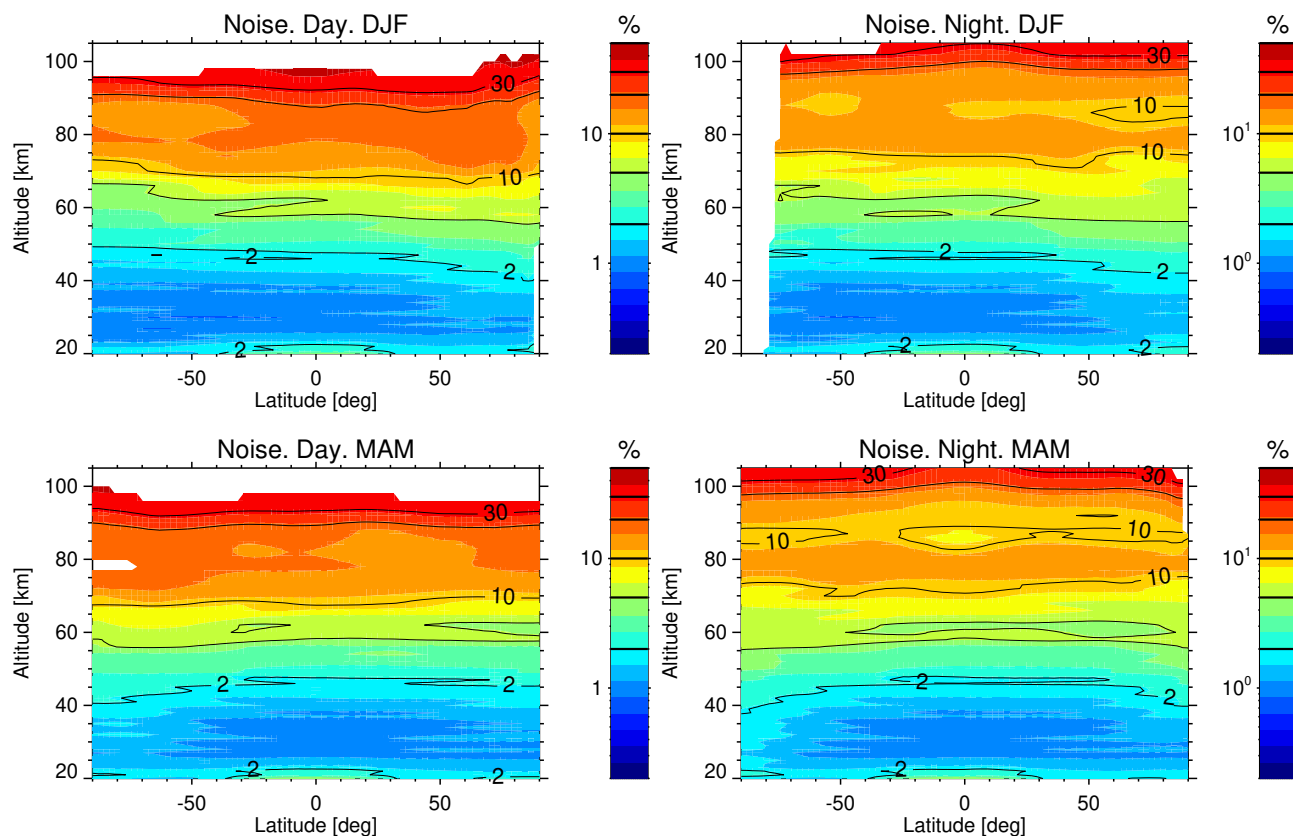
Figure 3. Latitude-altitude cross sections of the noise component of the ozone uncertainty in terms of estimated standard deviations for the MA mode. The left and right columns are for daytime and nighttime conditions, respectively. The top panels are for solstice conditions (Northern winter, December-January-February: DJF), and the bottom panels are for equinox conditions (Northern spring, March-April-May; MAM). The means span over all measurements from 2005 to 2012. White areas denote regions where the retrieved O_3 is not significant (AK diagonal <0.03). Contour lines are marked in the colour bar scale.

4 Error budget

275 The evaluation of the error budget of this version of ozone is based on the error estimation scheme for MIPAS version 8 data described by von Clarmann et al. (2022), which follows the TUNER (Towards Unified Error Reporting) recommendations. The novelty (and improvement) of this scheme is that it allows accounting for error correlations which may result in error compensation. Further, it also allows the error propagation of uncertainties in parameters obtained in preceding retrievals. The errors are estimated on a profile-by-profile basis for the measurement noise and on representative atmospheric conditions for

280 the rest of the errors. In particular, we considered 34 representative atmospheric conditions defined in terms of latitude band, season, and illumination conditions, which cover most of the climatologically expected situations for the middle atmosphere measurement mode (see Table A3 in von Clarmann et al., 2022). The attribution of a given measured profile to these representative atmospheres is given in Table A6 of von Clarmann et al. (2022). For some species, like NO, CO and CO_2, we also have to consider the upper atmosphere measurement mode scenarios and even also different solar conditions (Tables A4 and A5 in

285 von Clarmann et al., 2022). In the case of O_3, as its abundance is practically negligible above 105 km, the scenarios for UA are very similar to the middle atmosphere one. Hence we will focus on the error estimates for the latter but the estimates for both UA scenarios are also included in the supplement information for completeness.

In the next sections, we discuss the major error sources and the corresponding uncertainties that we assume in the estimation of the O_3 errors. Following the TUNER recommendations given by von Clarmann et al. (2022) we discuss, separately, the errors

290 thought to be of mainly random nature and those of systematic origin. The methodology of the error estimation for both types of errors is described in detail in von Clarmann et al. (2022). All estimated errors are given as standard deviations (1σ). A detailed analysis of the errors affecting the retrieved O_3 below about 70 km is already given in Kiefer et al. (2023). Nevertheless, for completeness, we briefly describe them here and focus on the middle/upper mesosphere and lower thermosphere where non-LTE errors are very relevant.

295 4.1 Error sources and uncertainties

Again, based on the nomenclature of von Clarmann et al. (2022), we considered the following types of errors: measurement errors, parameter errors, and model errors. The measurement errors comprise essentially the measurement (spectral) noise and additionally, those errors related to the instrument's state which are not well known (see Sec 4.1.1). Within the category of parameter errors fall the uncertainties of the atmospheric state parameters which are not known perfectly but not that much as

300 being considered as unknowns of the retrieval (see Sec 4.1.2). In this type, we also include those which cannot be retrieved from the measurements because they do not contain enough information about them. Lastly, we consider as model errors the uncertainties in the spectroscopic data and the non-LTE parameters (see Secs. 4.1.3 and 4.1.4). Note that the latter is specific to these atmospheric modes of observations and not included in the nominal mode.

4.1.1 Measurement errors

305 The measurement errors include the spectral noise of MIPAS, the uncertainty in the gain calibration, the instrument line shape uncertainty, inaccuracies in the frequency calibration and pointing errors.

The propagation of the spectral noise was estimated by using Eq. 5 of von Clarmann et al. (2022). The mapping of the other measurement errors on the O_3 error was evaluated from sensitivity studies performed for the representative atmospheric conditions discussed above.

310 The measurement noise is typically $30-33\,\mathrm{nW/(cm^2\,sr\,cm^{-1})}$ in the MIPAS A band and $5.4-9.6\,\mathrm{nW/(cm^2\,sr\,cm^{-1})}$ in the AB band. Both values refer to the apodized spectra. The mapping of those errors on the retrieved O_3 single profiles are shown in Fig. 3 for solstice conditions (top row) and equinox conditions (bottom row). As mesospheric O_3 is significantly different

during day and nighttime, and so is MIPAS sensitivity (see Fig. 2), we distinguish between daytime (left panels) and nighttime (right panels). Typical values (1σ) for daytime (left column of Fig. 3) are smaller than 5% below $\sim$60 km, 5–10% between 60 and 70 km, 10–20% at 70–90 km and about 30% at 95 km. For nighttime (right column of Fig. 3), the O_3 noise errors are very similar to those during daytime below around 70 km but significantly smaller above, being 10–20% at 75–95 km, 20–30% at 95–100 km (except near the tropics where the errors are smaller) and larger than 30% above 100 km.

The 1σ gain uncertainties were estimated to be 1.1% and 0.8% for the A and AB bands, respectively (see Kleinert et al., 2018). The response of retrieved ozone to the gain calibration is, to first order, multiplicative. Hence, in the band A spectral region, the gain uncertainties of the retrieved ozone mostly compensate for the gain uncertainty of the temperature and tangent altitude errors, since these are retrieved from the same band. This occurs approximately for the O_3 retrieved below about 50 km.

The instrument line shape (ILS) uncertainties and the spectral shift residual error have been evaluated as described in Kiefer et al. (2021) and are based on the estimates of modulation loss through self-apodization and its uncertainties. We also considered a residual frequency calibration error which resulted in 0.0003 cm^{-1} in bands A and AB.

4.1.2 Uncertainties in atmospheric parameters

In the ozone retrieval of the MA, UA and NLC modes we used the information of temperature and tangent altitude previously retrieved from the 15 μm region. Thus, the different sources of errors affecting the retrieved temperature and tangent altitude (T+LOS) are implicitly taken into account by propagating their uncertainties into the O_3 retrieval. The major sources of temperature are the following. The random component, mainly instrumental noise, is typically less than 1 K below 60 km, 1–3 K at 60–70 km, 3–5 K at 70–90 km, 6–8 K at 90–100 km, 8–12 K at 100–105 km and 12–20 K at 105–115 km (García-Comas et al., 2023). Its systematic part is dominated by the CO_2 spectroscopic data errors below 75 km and by the uncertainties in the non-LTE model parameters and CO_2 concentration above $\sim$80 km. The systematic uncertainties are smaller than 0.7 K below 55 km, 1 K at 60–80 km, 1–2 K at 80–90 km, 3 K at 95 km, 6–8 K at 100 km, 10–20 K at 105 km and 20–30 K at 115 km (García-Comas et al., 2023).

The uncertainties of the spectrally interfering molecules with ozone, i.e., N_2O, CH_4, NO_2, NH_3, HNO_3, ClO, OCS, HCN, CH_3Cl, H_2O_2, C_2H_2, C_2H_6, COF_2, C_2H_4, F-22, CCl_4, CFC-113, CFC-114, N_2O_5, HCFC-141B, HCFC-142B, $ClONO_2$, CH_3CCl_3, CH_3OH, acetone and PAN, which are not jointly fitted, as well as their vertical covariances, are estimated from the error covariance matrices of previous MIPAS data version V5R. These values are considered more accurate than the climatological mean values for the actual atmospheric conditions of the measurements. For those interfering species which are not available from previous MIPAS versions we used climatological data and estimate the effects of their errors on the retrieved O_3 from the perturbed spectra with their 1σ estimated uncertainties. We should note that, overall, the errors in O_3 due to the uncertainties in the interfering species are very small. This is due to the high spectral resolution of MIPAS which allows us to choose microwindows where essentially only O_3 contributes to the measured radiance. The errors caused by the uncertainties in H_2O are not explicitly included in the error budget as H_2O is jointly fitted with O_3 and H_2O uncertainties are implicitly taken into account during the propagation of measurement errors. Further, CO_2 uncertainties contribute to the O_3 error budget not only because of spectral CO_2 interferences (for which we also include CO_2 levels in non-LTE, see Sec. 2.2.4), but mainly

through its propagation via the preceding temperature retrieval from band A (see von Clarmann et al., 2022). CO_2 was taken from WACCM4 simulations and their 1σ uncertainties are listed in Table 3 of Kiefer et al. (2021).

In Section 2.2.4 we discuss the concentrations of the atomic oxygen and atomic hydrogen, which are not measured by MIPAS but required for the calculations of the non-LTE population of the O_3 levels. The atomic oxygen uncertainty contributes to the O_3 error budget in two ways. One, directly, through the non-LTE population of the emitting levels, as described above; and the other, indirectly through its impact on the kinetic temperature retrieval (see García-Comas et al., 2023). It is worthwhile to note that both errors partially compensate when propagated to the retrieved O_3. Thus, in the upper mesosphere, a larger [O] induces a larger retrieved kinetic temperature and hence a larger population of the O_3 emitting levels. On the other hand, a larger [O] gives rise to a larger collisional deactivation of the $O_3(v_1,v_3)$ levels and hence lower populations. In the lower thermosphere, the effects are swapped but with a similar compensating effect.

As described above, the daytime atomic oxygen is obtained from the retrieved O_3 below 95 km. It is then inherently retrieved together with O_3 and it is not by itself an independent source of errors. The uncertainties incurred by this approach are those introduced by the collisional and kinetic rates, which are described below in Sec. 4.1.4. During the nighttime, the [O] uncertainty is driven by that of atomic hydrogen. The uncertainties in [H] have been estimated by using Eq. (2) and the errors of the entering parameters which have been discussed above. They result in mean values ranging between 20 and 40% from 70 to 100 km, being larger in the tropics (40–60%) and smaller at high latitudes (10–30%).
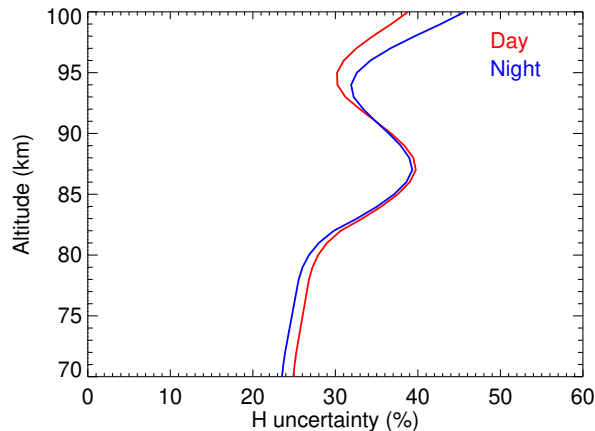
Figure 4. Mean of the [H] uncertainties included in the O_3 error budget for day and nighttime conditions.

In the region of 95–120 km, where [O] is taken from WACCM, we use the same uncertainties (5–30%) as those used in the kinetic temperature retrieval (see Fig. 6 in García-Comas et al. (2023)).

The "indirect" error induced by O through the temperature retrieval has been neglected. First, it is partially compensated by its direct effect on the populations of O_3. Secondly, the effect of the [O] error on the temperature uncertainty is much smaller than those of other parameters (e.g. of k_{CO2-O} (García-Comas et al., 2023)) already included. Further, we should note that

the propagation of the temperature errors onto O_3 is considerably weakened in the mesosphere since the emitting levels are in non-LTE, e.g., far away from the population dictated by the local kinetic temperature.

4.1.3 Uncertainties in spectroscopy

The spectroscopic errors are in general not so well characterised as it would be required for a thorough error assessment of remotely sensed data. In particular, neither any information on the confidence limits (e.g. 68%, 95% or other) of the error margins (1σ or 2σ), nor about error covariances between spectral lines and bands is available. The spectroscopic errors for O_3 are described in detail by Kiefer et al. (2023); see Table 2 in that work. In summary, for the stronger ozone lines, we assume uncertainties in their intensities in the range of 2–4%. The broadening coefficients were parameterised as a function of the rotational quantum number and their uncertainties vary from 3.5%, 7.5%, 15%, to 20%, depending on the considered ozone band. In this respect, we were rather conservative and assumed that all errors in the lines of a given band are completely correlated.

4.1.4 Uncertainties in non-LTE parameters

The uncertainties in the non-LTE model are an important source of systematic error for O_3 above the mid-mesosphere. Their most important components are the uncertainties in the collisional rates and, as discussed above, uncertainties in the atomic oxygen concentration. The errors of the collisional rates were discussed in López-Puertas et al. (2018) and their values have not changed in this version. In summary, we considered an uncertainty of: 1) 10% for the three-body reaction rate of O_3 formation (k_1 in Table 1); 2) 20% for the thermal relaxation of $O_3(v_1, v_3)$ by N_2 and O_2; and 3) 50% for the collisional relaxation (and/or chemical reaction) of $O_3(v_1, v_3)$ with atomic oxygen (k_3 in Table 1), the latter based on West et al. (1976, 1978). The error of the photo-absorption coefficient J_{O3}, required in the photochemical model described above, was estimated to be 7%.

4.2 O_3 error estimates

While in the preceding section various contributions to retrieval uncertainties were reported, here we assess their effect on the retrieved ozone mixing ratios. As discussed above we distinguish between the errors which are mainly random and those of a predominantly systematic nature. All error components, both random and systematic, contributing to the O_3 error budget for the considered 34 atmospheric conditions are given in the supplement document. Tables S2–S35 and Figs. S1–34 refer to MA measurements while Tables S37–S70 and Figs. S35–S68 refer to UA measurements. Fig. 5 shows three examples for the middle atmosphere (MA) mode corresponding to the tropics, to northern mid-latitudes and to polar summer and polar winter conditions. The results are shown for daytime and nighttime conditions because mesospheric ozone is very different for those situations. Some numeric values at selected altitudes and conditions are given in Tables B1–B6 for easier reference. They also list mean O_3 vmrs which can help in estimating absolute O_3 errors from the given relative errors.

Many error components cause both a bias and scatter and thus contribute to the random and the systematic error budget. In Fig. 5, the combined random and systematic error is shown for each error source. Both, propagated measurement noise
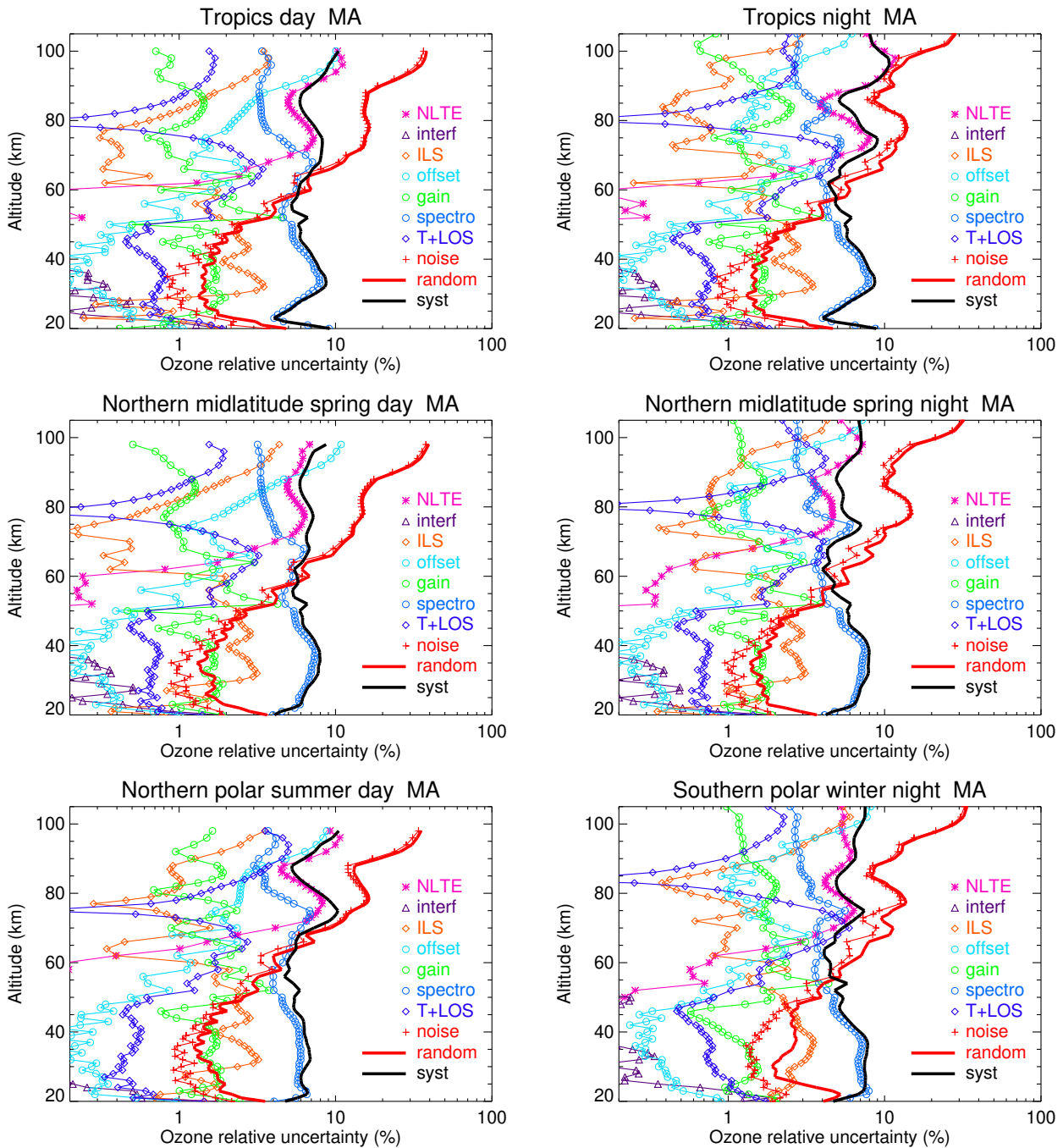
Figure 5. O₃ error budget for MA data for different atmospheric conditions (top to bottom) tropics, northern mid-latitudes in spring and polar regions, for daytime (left column) and nighttime (right column). All error estimates are 1σ uncertainties and are given in percent. Error contributions are labelled "T+LOS" for the propagated error from the T+LOS retrieval, "noise" for error due to measurement noise, "spectro" for the spectroscopic error, "gain" for gain calibration error (see text), "offset" for error due to spectral offset (see text), "ILS" for instrument line shape error (see text), "interf" for the uncertainty in the abundance of the interfering species, and "NLTE" for non-LTE related errors. The total random ("random") and systematic ("syst") errors are also shown.

and noise-induced T+LOS errors are considered as purely random. Some error sources affect the ozone retrieval via multiple pathways. First, the error affects T+LOS, and the resulting T+LOS error is further propagated on O_3. Secondly, the same error affects the O_3 retrieval directly. For example, too large radiances due to less-than-perfect gain calibration lead to high temperatures that cause lower retrieved O_3 mixing ratios. Along the second pathway, too large radiances in the O_3 band cause also higher retrieved O_3 mixing ratios. In the figures, we show the net effect of both pathways, labelled by the respective error source, while the error component labelled 'T+LOS' contains only the ozone error due to the propagated noise-induced T+LOS error.

In the next sections we assign the error components to the random versus systematic category and discuss their relevance. An exception is non-LTE errors, which are very relevant in the mesosphere and above. They are analyzed in a separate section, where both their random and systematic components are discussed together.

4.2.1 Random errors

In line with the recommendation of TUNER, we consider as random errors those that explain the standard deviation of the differences of collocated measurements taken by two instruments of the same state variable (von Clarmann et al., 2022).

We identified the following error sources as contributing to the random error: measurement noise, gain calibration uncertainties, offset calibration noise, T+LOS errors, uncertainties in the abundance of interfering species, and the residual frequency calibration errors. Further, we also include in the random error the random variations of retrieval responses to systematic uncertainties (so-called "headache errors", see von Clarmann et al., 2022).

The random component of the errors in Fig. 5 are shown in Fig. C1. The major component of the random error is measurement noise. Zonal mean distributions of the ozone error due to noise for solstice and equinox, and for daytime and nighttime, have been discussed above in Sec. 4.1.1 and are shown in Fig. 3. The noise error (+) and the total random error (thick red line) (see Fig. 5) are practically overlaid above ∼70 km, reflecting the predominance of noise in the random error budget at these altitudes. Above ∼80 km, some further contributions are made by the offset uncertainty, the random component of the NLTE error, and for some atmospheric conditions, the random component of the propagated T+LOS error. Between ∼70 km and ∼50 km, the propagation of the temperature and LOS random errors significantly contribute. Below ∼50 km, both T+LOS errors and the random component of the spectroscopic errors contribute significantly to the total random error.

The random component of the gain calibration error is very small and the values shown in Fig. 5 are mainly of systematic nature. The errors induced by the uncertainties in the abundance of interfering species are significant only below about ∼30 km. Errors produced by the residual frequency calibration uncertainty are negligibly small and are not shown.

The total random error varies between ∼1–2% near 30 km, and increases with altitude reaching 20%–30% in the upper mesosphere/lower thermosphere. In this region, it is larger at daytime than at nighttime. In the lower stratosphere, due to the temperature decrease, it also increases (see more details in Kiefer et al., 2023). The random O_3 error is generally larger than the total systematic uncertainty above around ∼60 km.
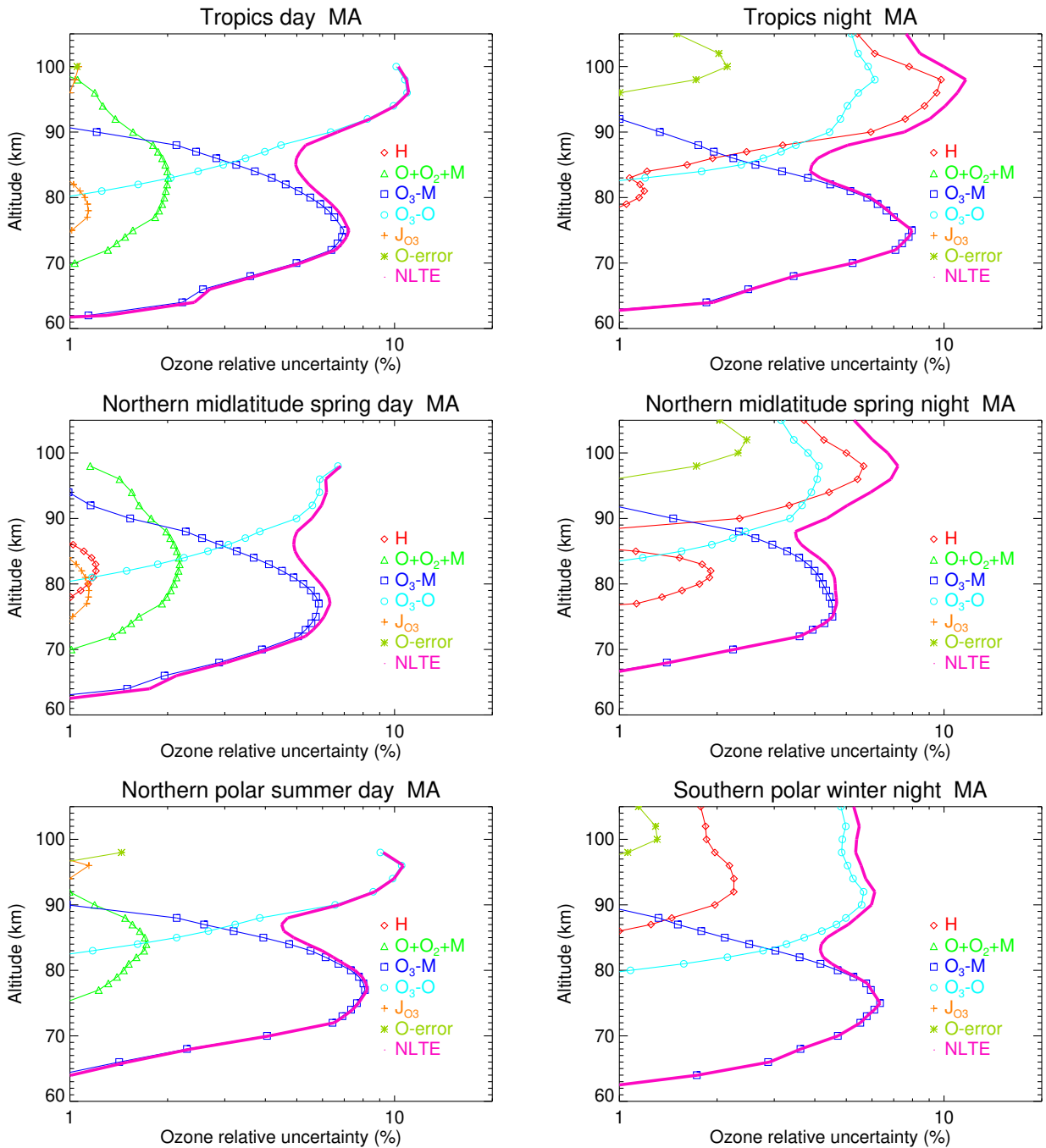
Figure 6. O_3 non-LTE error budget for MA data for different atmospheric conditions (top to bottom) tropics, northern mid-latitudes in spring and polar regions, for daytime (left column) and nighttime (right column). All error estimates are 1σ uncertainties and given in percent. Error contributions are labelled as: 'H' the error due to [H], 'O+O$_2$+M' the error due to k_1, 'O$_3$-M' error due to $k_{vt,M}$, 'O3-O' the error of $k_{vt,O}$, 'J_{O3}' the error of the photo-absorption coefficient J_{O3}, 'O-error' the error of [O] above $\sim$95 km, and "NLTE" is the total non-LTE contribution. See Table 1 for the different rates and their assumed errors.

4.2.2 Systematic errors

The sources of systematic errors in MIPAS O_3 retrievals from middle atmosphere measurements are: uncertainties in spectroscopic data, instrument line shape uncertainties, the gain calibration error, and non-LTE related uncertainties. The systematic component of the errors in Fig. 5 are shown in Fig. C2. The systematic error is dominated by the spectroscopic data error below $\sim$60 km. In this region, the ILS also contributes significantly and, to a lesser extent, the gain calibration uncertainty. Above $\sim$60 km the systematic errors are dominated by the non-LTE uncertainties, which are discussed below, but the spectroscopic data error also contributes significantly, being in some cases comparable or even larger than the non-LTE errors. The ILS contribution is also appreciable at very high altitudes, above $\sim$90 km.

4.2.3 Non-LTE errors

The non-LTE error includes both uncertainties of the collisional and kinetic rate constants as well as uncertainties in the abundances of atmospheric species required for the non-LTE modelling, namely, atomic oxygen (O) and hydrogen (H). Abundances of these species are uncertain due to uncertainties in the kinetic constants of the photochemical model used to infer them, or by biases in the trace gas climatologies used. Both errors are primarily systematic, i.e., bias-generating, while their random component is less relevant. Only in a few conditions and altitudes the random component of the non-LTE is significant, e.g., near 95 km during daytime in the tropics and in the northern polar summer (see Fig. 5).

The different components of the non-LTE errors corresponding to the atmospheric conditions of Fig. 5 are shown in Fig. 6. Non-LTE errors are only significant above $\sim$70 km and are in the range of 1% to 10%. In the region of 65–85 km the non-LTE error is dominated by the uncertainty in the thermal relaxation of $O_3(v_1, v_3)$ by N_2 and O_2, process 5, $k_{vt,M}$, in Table 1, and above $\sim$85 km by the errors in the collisional relaxation reaction of $O_3(v_1, v_3)$ with atomic oxygen, process 6, $k_{vt,O}$, in Table 1, and by uncertainties in the abundances of atomic hydrogen. The latter is the largest contributor above $\sim$90 km during nighttime conditions at tropical and mid-latitudes. The error component due to atomic oxygen abundances in the region where it is not retrieved ($z \gtrsim 95$ km) contributes moderately at the highest altitudes. The error contribution of the reaction rate of O_3 formation (k_1 in Table 1) is negligible during nighttime and below 2% during daytime. The error due to the photo-absorption coefficient is hardly 1% near 80 km during daytime. Overall, the non-LTE errors are typically negligible (smaller than 1%) below 60 km, 2–8% at 60–85 km, and slightly larger, 5–12% above 85 km.

5 Differences between current V8R_O3_m61 and previous V5R_O3_m22 O_3 data

The average impact on the ozone retrieval after including the changes discussed in Sec. 2, i.e., differences between the current data version V8R_O3_m61 and the previous version V5R_O3_m22, is an increase of 2–5% (0.2–0.5 ppmv) below around 50 km (see Figs. 7 and 8a). Also, there is a clear decrease by $\sim$2–4% between 50 and 60 km, mainly in the tropics and mid-latitudes (see Fig. 8b). In the region between 70 and 85 km we observe an oscillating behaviour of the differences with
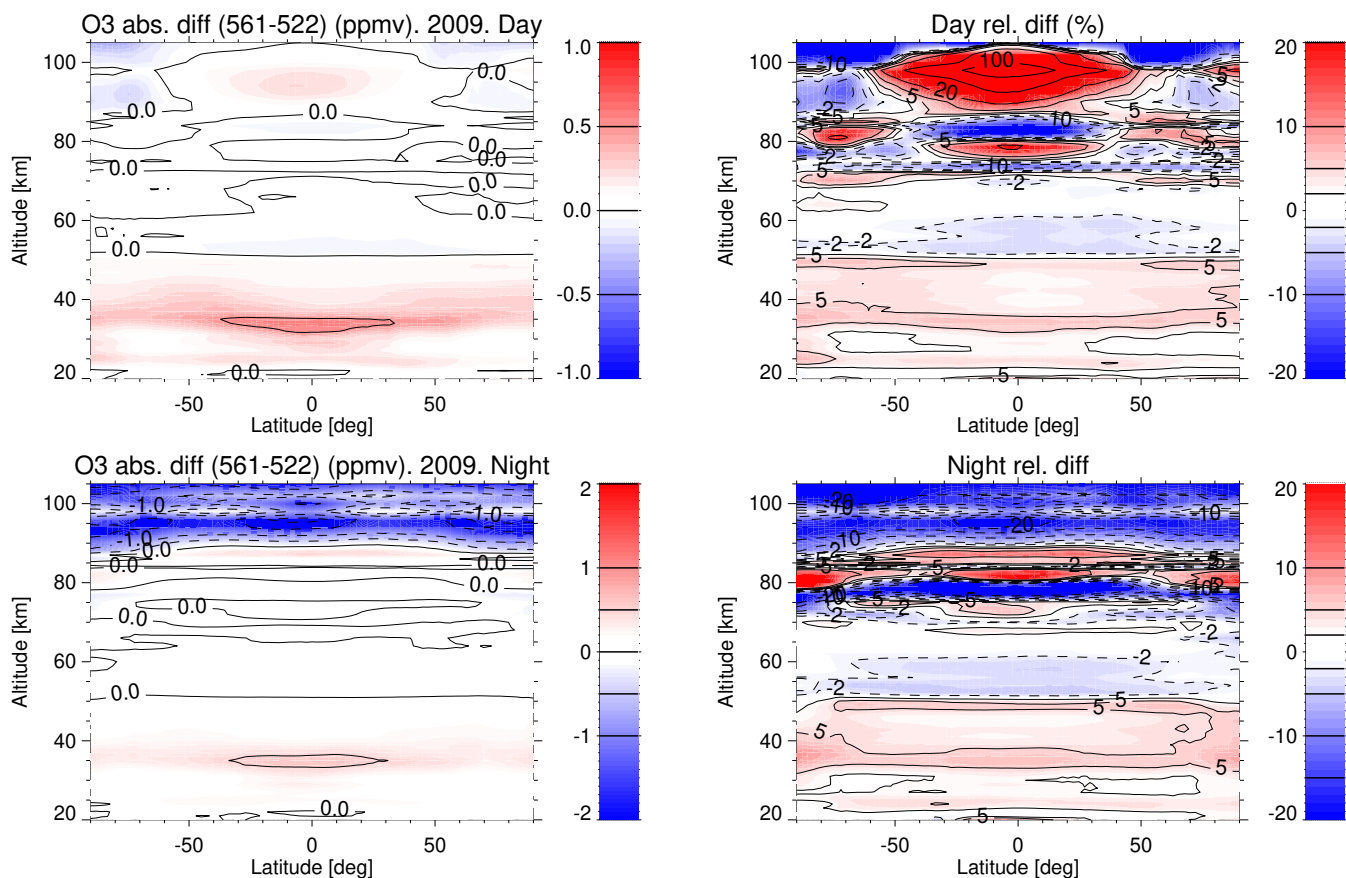
Figure 7. Comparison of O_3 abundance retrieved in the V8R_O3_561 with the previous V5R_O3_522 version for daytime conditions (10 am) (top) and nighttime (bottom). The plots show the mean of the differences, in % of the older version, (V8R_O3_561–V5R_O3_522)/V5R_O3_522, for all data taken in 2009. Note that in the upper/right panel there are two contours, 50% and 100%, which are beyond the colour scale. That is, differences larger than 20% are coloured with the brightest red.

amplitudes smaller than ∼10%. The concentration of O_3 at these altitudes is very small (below ∼0.5 ppmv); hence these differences are not of much importance in absolute terms (see left panels of Fig. 7).

The position and magnitude of the O_3 tertiary maximum, located near 70 km at high winter latitudes, are very similar in both versions, with no significant difference. This can be seen, e.g., in a comparison between panels (d) and (f) in Fig. D5 with the corresponding panels in Fig. 15 of López-Puertas et al. (2018).

The nighttime O_3 minimum just below 80 km is more pronounced in the new version. This is seen in the right/bottom panel of Fig. 7 and in Fig. 8c, as well as in a comparison of panel (b) in Fig. D5 with the corresponding panel in Fig. 15 of López-Puertas et al. (2018). Nevertheless, it is interesting to note that the O_3 fields near 78 km show larger values at daytime than at nighttime (see Figs. 8c and D3). This day/night difference is of a different sign than in the previous version (see Fig. 13 in López-Puertas et al., 2018) but is in agreement with both SABER measurements and WACCM predictions (see López-Puertas

et al., 2017). Hence, the new O_3 dataset in this region seems to have improved and shows a more realistic diurnal variation in the mesosphere.
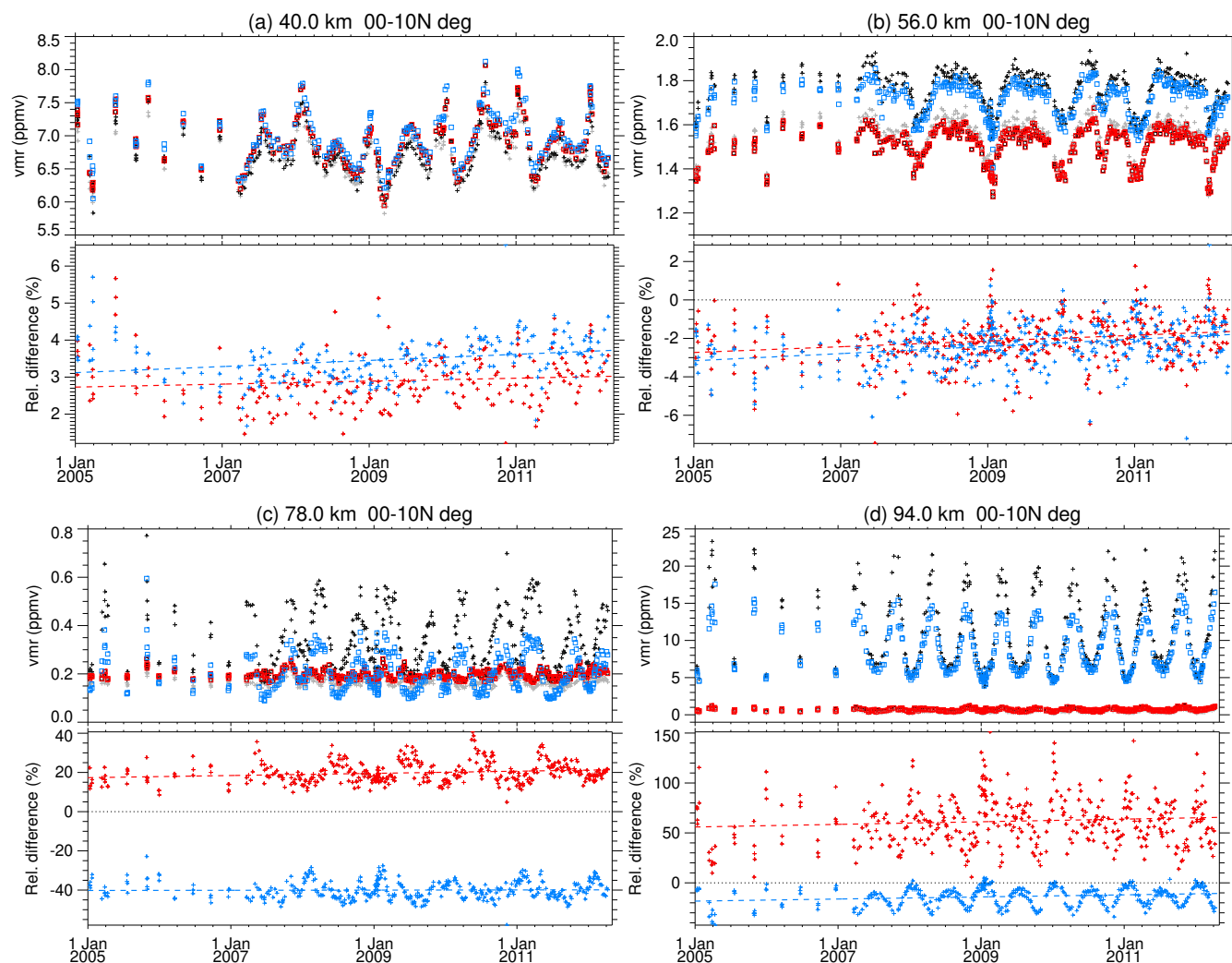
Figure 8. Comparison of O_3 abundance retrieved in the V8R_O3_561 version with that in the previous V5R_O3_522 version for daytime (10 am) (red, light pluses) and nighttime (blue, dark pluses). Squares: V8R_O3_561; pluses: V5R_O3_522. The top and bottom panels show the time series of O_3 vmr and of the relative differences, (V8R_O3_561–V5R_O3_522)/V5R_O3_522, respectively. Figures a–d are for 40 km, 56 km, 78 km, and 94 km, respectively, all for 0–10°N.

The O_3 concentration in the secondary maximum during daytime in the tropics and midlatitudes is about 40% larger in the new version compared to the previous version (see top/right panel of Fig. 7 and Fig. 8d). In absolute terms, this difference amounts at 0.2–0.3 ppmv only. The daytime secondary maximum is also situated about 1–2 km higher than in the previous version (e.g. compare panel (a) in Fig. D5 with the same panel in Fig. 15 of López-Puertas et al., 2018). The cause of these

differences is the use of a different a priori O_3, the WACCM-corrected fields instead of the values of the Garcia and Solomon (1994) model, together with the relatively low vertical resolution of MIPAS in this region for daytime (see left panels of Fig. 1). This effect outweighs the smaller O_3 values expected from the lower photo-absorption coefficient J_{O3} and the lower de-activation rate of the $O_3(v_1,v_3)$ states by atomic oxygen (see Sec. 2)

The most significant change in the mesosphere occurs at nighttime in the secondary maximum, where O_3 in the new version is reduced between 10–30% (see bottom/right panel in Fig. 7 and Fig. 8d). This is caused mainly by the lower collisional relaxation/chemical removal rate of the $O_3(v_1,v_3)$ states by atomic oxygen, a factor of two smaller (see Sec. 2.2.3). This feature can also be appreciated very clearly when comparing Fig. D2 and Fig. 12 in López-Puertas et al. (2018), particularly near the tropics during equinox conditions, when the maximum of O_3 occurs. Further, the reduced ozone abundances in the secondary maximum during nighttime is also evident when comparing panels (b) in Fig. D5 and in Fig. 15 of López-Puertas et al. (2018).

6 Consistency between nominal and middle atmosphere O_3 data

In order to obtain comprehensive long-term datasets for studying possible changes and trends of atmospheric state variables, it is often necessary to rely on data from different sources. In that sense, the NOM and MA/UA MIPAS O_3 datasets can be used in combination. For this purpose, it is important to know the consistency between these datasets. The NOM dataset has the advantage that measurements were taken more frequently. These measurements, however, cover a limited altitude range and include non-LTE, which is expected to be important in the 50–70 km altitude range, in an approximate way only (Kiefer et al., 2023). In contrast, the MA/UA V8R dataset described here covers a wider altitude range but is rather discontinuous in time. Only about one of ten days was reserved for each of these measurement modes. Differences between both datasets are shown in Fig. 9 for four seasons and separately for 10 am and 10 pm. The general pattern is that both datasets seem to be very consistent. Differences are generally within 1–2%. The larger differences appear in the lower mesosphere (60–70 km) during daytime where NOM O_3 concentrations seem to be generally by about 2% to 10% larger than those of the MA/UA dataset for most latitudes. These differences are attributed to a more accurate account of non-LTE, known to be more pronounced in the daytime. One clear exception to that general feature is the tertiary maximum occurring near 60–70 km under polar winter conditions (near the North pole during DJF and close to the South pole in JJA). In these regions, MA/UA O_3 concentrations are larger by $\sim$5–10%. A similar situation occurs near the South Pole for MAM, where MA/UA O_3 abundances are also larger. A candidate explanation for these differences is that NOM retrievals are not including appropriately the O_3 field above its uppermost tangent height of the measured spectra ($\sim$70 km). There are also other patches at high latitudes and at different altitudes where the NOM O_3 concentrations are slightly larger by 2–3% than those of MA/UA, but these are small and do not appear to be systematic.
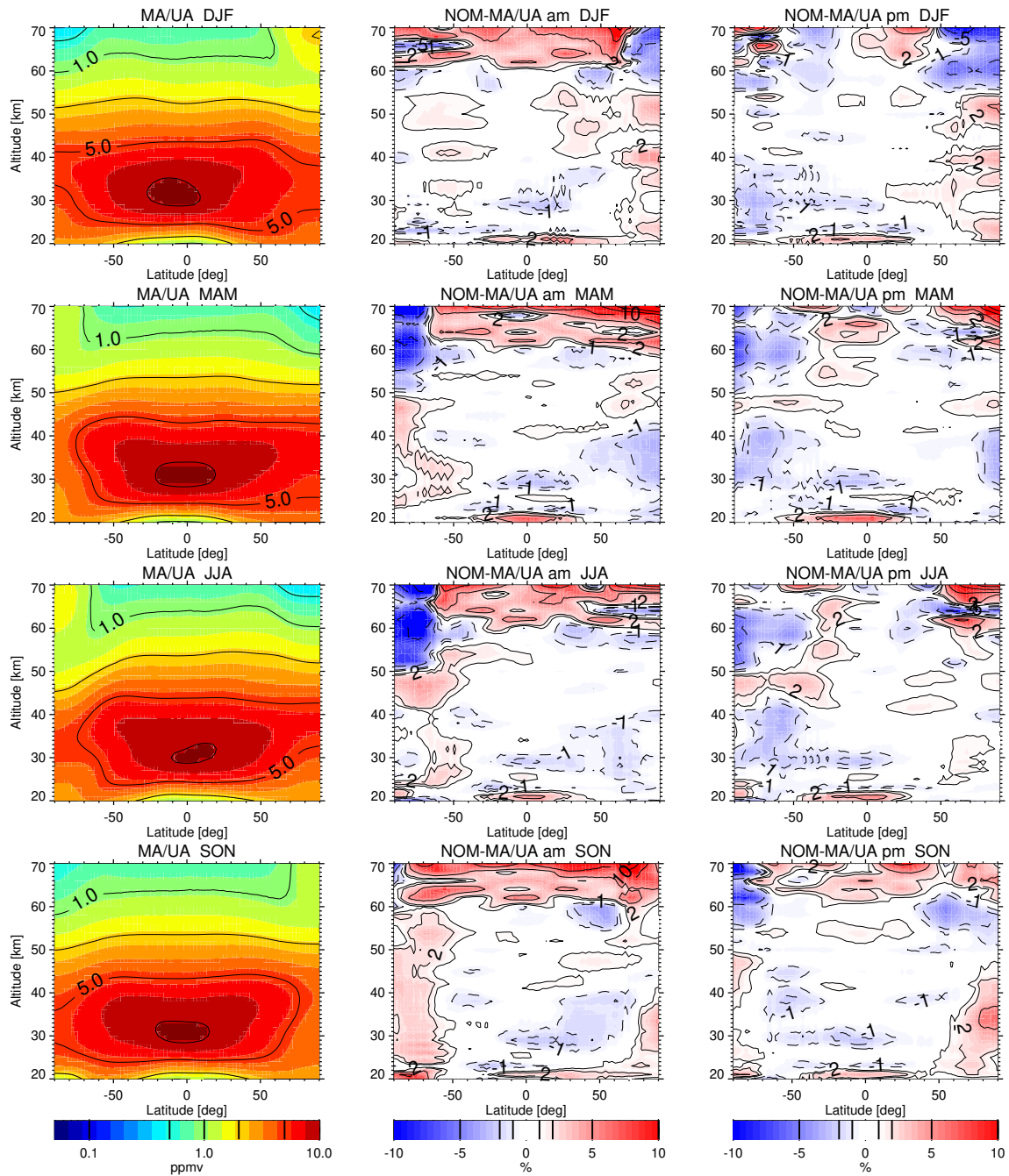
Figure 9. Comparison of O_3 zonal mean abundances retrieved in the V8R MA and UA data with the V8R NOM data for four seasons (rows). From top to bottom, for the Northern winter season (December–February, DJF), for the Northern spring (March-May, MAM), for the Northern summer winter (June-August: JJA) and for Northern autumn (September-November, SON). The left panels show the zonal mean of V8R MA/UA data, including 10 am and 10 pm. The central and right panels show the NOM–MA/UA differences for daytime (10 am) and nighttime (10 pm). The averages cover the measurements taken from 2006 through 2011.

7 Comparison with other satellite measurements

We have compared MIPAS retrievals of this new version of O_3, V8R_O3_m61, with co-located measurements from SABER, GOMOS, MLS, SMILES and ACE-FTS in a similar way as we did for the previous version (López-Puertas et al., 2018). We have used more recent data versions from MLS and ACE-FTS.

Comparisons for GOMOS are only for night conditions and are performed in number density. For ACE-FTS, because it is an occultation instrument and O_3 has very large diurnal variations around the terminator in the middle and upper mesosphere, we compare ACE sunset and sunrise with MIPAS observations taken at solar zenith angles (SZA) from 88° to 92°. We kept the same co-location criteria as in the previous version, e.g., we selected pairs of profiles of the different instruments with Universal Time differences smaller than 2 h and distances smaller than 1000 km.

7.1 Instruments

7.1.1 SABER

SABER (Sounding of the Atmosphere using Broadband Emission Radiometry) is a broadband radiometer flying onboard NASA's Thermosphere-Ionosphere-Mesosphere Energetics and Dynamics (TIMED) satellite, launched on December 2001 and starting operations in January 2002 (Russell III et al., 1999). It measures from 83°S to 52°N and from 52°S to 83°N, alternatively every two months. A 24-h local time coverage is completed in ∼60 days. The instrument measures the ozone limb emission at 9.6 μm during daytime and nighttime, and the ozone concentration is retrieved from 10 to 100 km using a non-LTE model (Mlynczak et al., 2013). Here we use version 2.0 of O_3 retrieved from the 9.6 μm channel, publicly available at http://saber.gats-inc.com. SABER's ozone precision is ∼1–2% in the stratosphere and ∼3–5% in the lower mesosphere (Rong et al., 2009). The systematic errors range from 22% in the lower stratosphere to ∼10% in the lower mesosphere. The vertical resolution of SABER ozone is approximately 2 km. Given MIPAS O_3 coarser vertical resolution, particularly in the daytime mesosphere, we used the MIPAS averaging kernels and a priori O_3 to smooth SABER O_3 profiles.

7.1.2 GOMOS

The Global Ozone Monitoring by Occultation of Stars (GOMOS) instrument was a stellar occultation spectrometer onboard the ESA's Envisat space platform (Bertaux et al., 2010) and operated from August 2002 to April 2012. GOMOS took measurements at $250-692$ nm and O_3 nighttime density profiles were derived from 10 to 110 km. The latitudinal coverage is uneven providing data at low latitudes at around $22-23$h LST and eventually reaching the poles and slightly varying throughout the year. We used here the ESA IPF version 6.01 which is described in Kyrölä et al. (2010) and Sofieva et al. (2010). These data are available from the ESA Earth online portal (https://earth.esa.int). Unreliable profiles have been removed following the recommendations of the GOMOS/6.01 Level 2 Product Quality Readme file.

GOMOS O_3 vertical resolution changes from 2 km in the lower stratosphere to 3 km in the upper stratosphere and above. Because this resolution is better than that of MIPAS, we applied MIPAS averaging kernels to the GOMOS profiles. Because

GOMOS provides O_3 number density we compare the GOMOS and MIPAS O_3 number densities. Random errors due to measurement noise and scintillations are $0.5-4\%$ in the stratosphere and $2-10\%$ in the mesosphere. Systematic errors are smaller than 2%, mainly induced by the O_3 spectroscopic data (Tamminen et al., 2010).
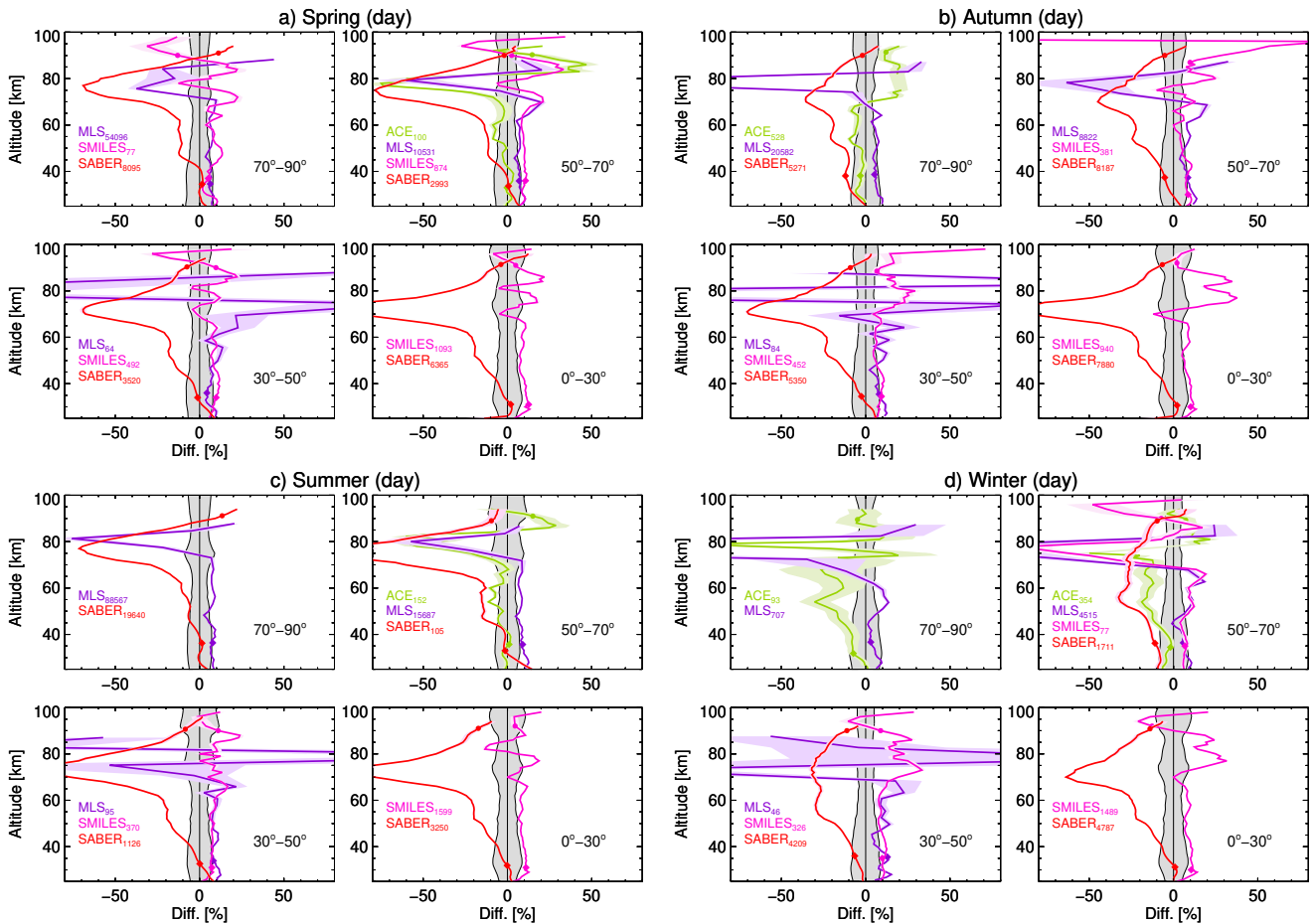
Figure 10. Mean of the daytime O_3 vmr differences (MIPAS–instrument) in % of MIPAS between co-located pairs of measurements of MIPAS (MA mode) with ACE-FTS (green), MLS (purple), SMILES (magenta) and SABER (red) for a) spring (MAM for NH and SON for SH), b) autumn (SON for NH and MAM for SH), c) summer (JJA for NH and DJF for SH), and d) winter (DJF for NH and JJA for SH). The symbols indicate the mean altitude of the MIPAS O_3 vmr primary (diamonds) and secondary (circles) maxima coincident with the respective instrument. The number of coincidences is indicated in the subscripts. The colour-shaded areas (hardly noticeable in many cases) are the standard errors of the mean of the differences. The grey shaded area shows the MIPAS 1σ systematic errors (e.g. curve 'syst' in Fig. C2).

7.1.3 MLS

The Microwave Limb Sounder (MLS) was launched on July 2004 on NASA's Earth Observing System Aura satellite (Waters et al., 2006). The ozone dataset used here is version 5.0-1.1a, downloaded from GES DISC (Schwartz et al., 2015) and described
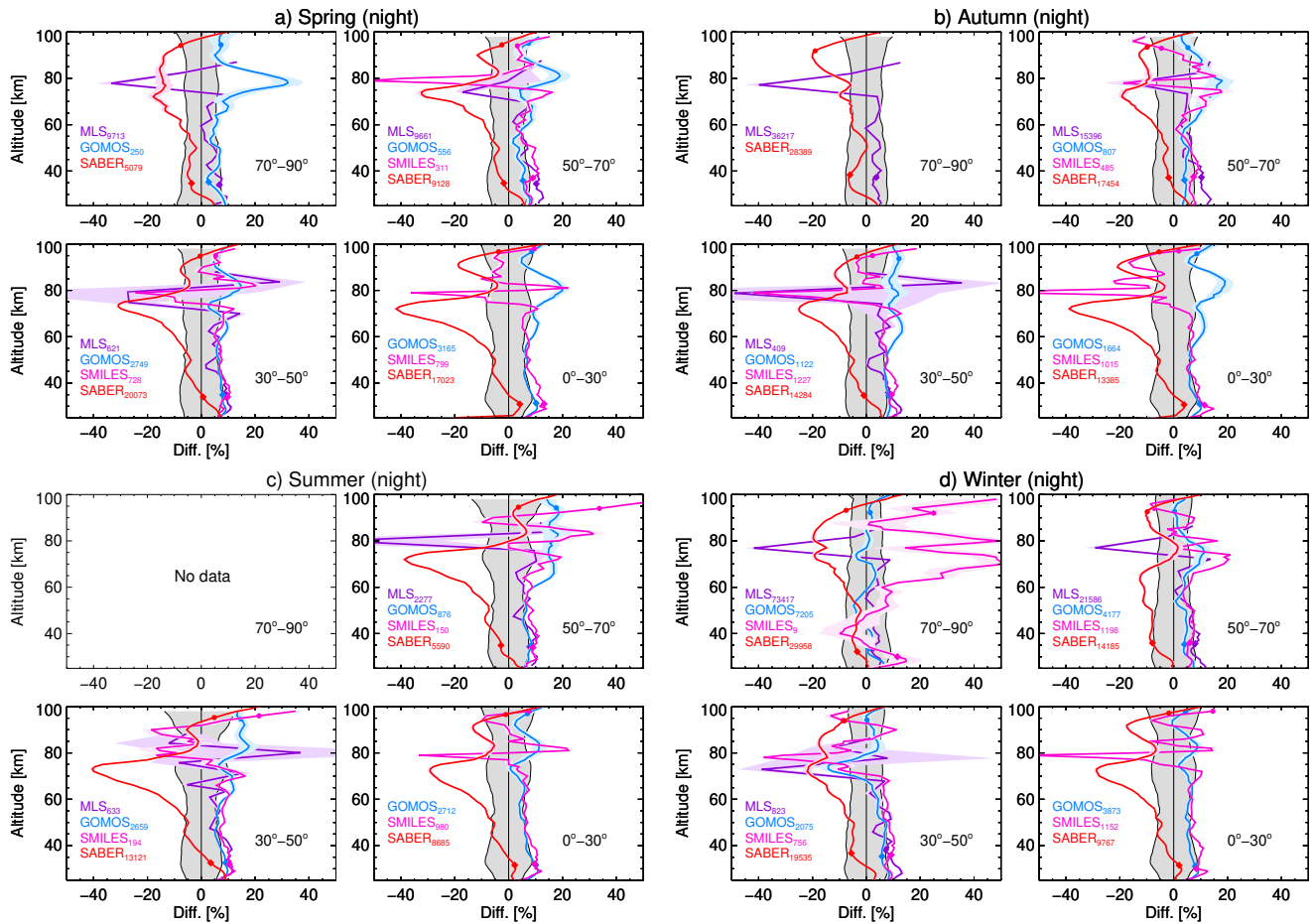
Figure 11. As Fig. 10 but for nighttime O$_3$. Instruments colours are the same except that ACE-FTS is replaced by GOMOS (light blue).

by Livesey et al. (2022). "One of the major differences of this data version compared to previous ones is that the ozone retrieval
545 uses larger a priori errors at high altitudes, making the retrieved O$_3$ less dependent on the a priori. Thus, it can be used up to
higher altitudes, to 0.002 to 0.001 hPa ($\sim$90 km). We used here daytime and nighttime O$_3$ profiles from the stratosphere up
to 0.001 hPa ($\sim$90 km, see https://mls.jpl.nasa.gov). This is an important difference with respect to the previous comparison
carried out by López-Puertas et al. (2018), where it was limited to $\sim$72 km.

The vertical resolution of MLS ozone profiles is 3 km in the stratosphere, 6 km in the middle mesosphere and 9 km in the
550 upper mesosphere. The estimated systematic uncertainty is 5–10% in the stratosphere, 10–20% in the lower mesosphere and
20–40% in the middle mesosphere (with a larger error of 100% near 80 km) (see Table 3.18.2 in Livesey et al., 2022). Since
the MLS O$_3$ vertical resolution in the mesosphere is larger than that of MIPAS, we have applied MLS averaging kernels and a
priori information to the MIPAS ozone.

7.1.4 SMILES

The Superconducting Submillimeter-Wave Limb-Emission Sounder (SMILES) on the International Space Station (ISS) operated between October 2009 and April 2010 (Kikuchi et al., 2010). It measured ozone profiles in the altitude range of 16 to 85 km during daytime and up to 96 km during nighttime (Mitsuda et al., 2011; Takahashi et al., 2010, 2011). The latitudinal coverage is 38°S and 65°N. Data version 3.2 was used here (http://darts.isas.jaxa.jp/stp/smiles/). The vertical resolution is 3 km in the stratosphere, 4 km in the lower and mid-mesosphere and 6 km at 95 km. MIPAS and SMILES O_3 vertical resolutions are similar and hence no averaging kernels were applied. Previous versions of SMILES O_3 (v2.2) agree with other measurements within 10% in the stratosphere and 30% in the mesosphere (Imai et al., 2013a,b).

7.1.5 ACE-FTS

The Fourier Transform Spectrometer (ACE-FTS) is an infrared solar occultation Michelson interferometer flying on the CSA's Atmospheric Chemistry Experiment (ACE), launched in August 2003 (Bernath, 2017). It measures atmospheric absorption from the cloud top to 150 km at sunrise and sunset. ACE covers the tropical, mid-latitude and high-latitude regions in approximately three months. Ozone profiles are retrieved from microwindows between 829 and 2673 cm^{-1} (Boone et al., 2013). We use here data version 4.1. ACE-FTS ozone retrievals are limited to a 5–95 km altitude range. The vertical resolution is $3-4$ km.
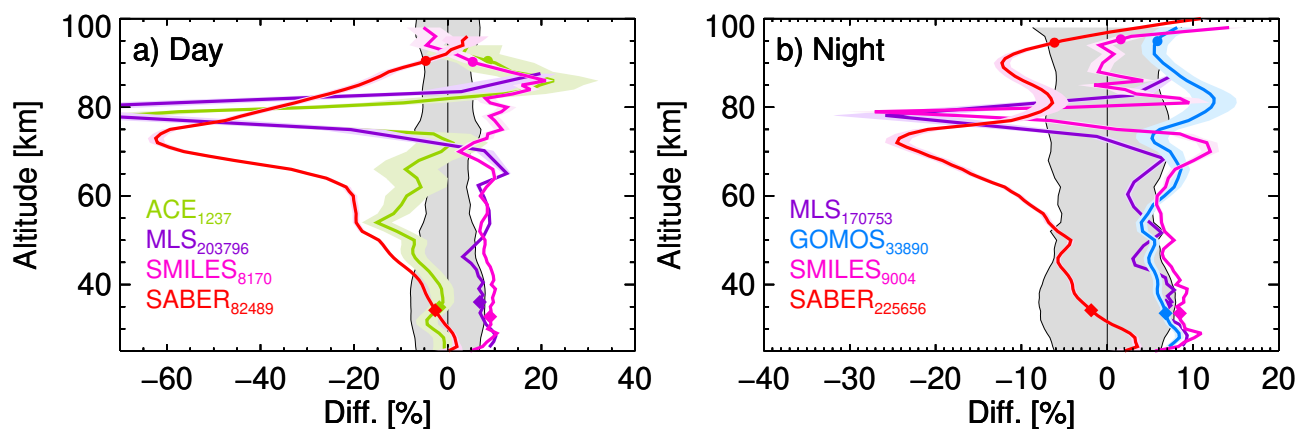
Figure 12. Global mean (for all latitudes and seasons) of the daytime O_3 vmr differences (MIPAS–instrument) in % of MIPAS between co-located pairs of measurements of MIPAS (MA mode) with ACE-FTS (green), MLS (purple), SMILES (magenta), SABER (red) and GOMOS (light blue). For more details see the caption of Fig. 10.

7.2 Results of the comparison

Figures 10 and 11 show the mean daytime and nighttime differences, respectively, between MIPAS and the different instruments (MIPAS−instrument) for the four seasons, grouped in four latitude bins. Further, the global mean differences, including all

latitudes and seasons, are plotted in Fig. 12, separated in daytime and nighttime. We have shown the systematic errors of MIPAS just as a reference.

We see that MIPAS compares very well with ACE in the stratosphere and lower mesosphere (up to 75 km) with differences smaller than 5%, except for a narrow region close to 55 km where ACE is larger by about 10%.

The comparison with MLS and SMILES in this region is very consistent, with MIPAS O_3 mixing ratios being in general larger, between 5% and 10%, than those of these two instruments up to altitudes of nearly 75 km. Note that the differences with respect to MLS at nighttime in this region are slightly smaller, with values close to 5% from 45 km to 75 km. The better agreement between infrared (MIPAS and ACE) instruments with respect to the microwave instruments (MLS and SMILES) suggests that the differences are caused by inconsistencies between the spectroscopic data in those spectral regions. In fact, it has been shown that O_3 intensities in HITRAN 2016 (the basis of ACE v4 retrievals) are too weak by about 3% (Birk et al., 2019). This bias, although does not fully explain the differences between ACE-FTS and MLS/SMILES of about 5–10%, is consistent with this result.

MIPAS agrees well with SABER in the lower stratosphere, up to $\sim$35 km. However, above this altitude, at 40 to 60 km, SABER O_3 vmr is larger than MIPAS by 20% during daytime and by 10% at nighttime. The differences are larger for MLS, SMILES and GOMOS. Rong et al. (2009) found a positive bias in SABER stratospheric O_3, version 1.07, which might explain these differences. Also, SABER retrieves O_3 from the bands in the 10 μm region while MIPAS uses up to 50 km the v_2 band. We have discussed above that when using the microwindows of MIPAS AB band, which include lines of the ozone 10 μm band, we retrieve larger O_3 concentrations. Thus, these spectroscopic inconsistencies might partially explain the MIPAS and SABER differences in this region. Above 60 km, the differences between MIPAS and SABER increase, reaching differences at 60–85 km within 20–60% at daytime, and in the range of 10–25% at nighttime, with MIPAS ozone mixing ratios being always smaller. Smith et al. (2013) have already reported that daytime SABER O_3 mixing ratios are overestimated in this region. One possible cause of this overestimation is the larger collisional rate (about a factor of two) for the $O_3(v_1,v_3) + M(N_2, O_2)$ process used in SABER as compared to MIPAS retrievals (Mlynczak et al., 2013; López-Puertas et al., 2018). This would also explain the larger differences at daytime as non-LTE effects are larger for these conditions (Funke et al., 2012).

The large relative differences of MIPAS with respect to ACE and MLS near 80 km are caused by the smaller concentrations of O_3; the difference in absolute values is smaller than 0.1 ppmv. MIPAS, however, shows slightly larger ($\sim$10%) O_3 vmr than SMILES in this region. In the daytime upper mesosphere, near 85–90 km, it seems that MIPAS has a positive bias of 10 to 20% with respect to ACE, MLS and SMILES, although it is smaller than the SABER O_3 by similar amounts. However, the agreement between all instruments near the secondary maximum is remarkably good.

The differences between the instruments for nighttime conditions in the stratosphere and lower mesosphere (Fig. 12b) are consistent with the daytime differences. The nighttime data were also compared to GOMOS data. This comparison seems to corroborate the differences found with MLS and SMILES.

Near 60–70 km, the agreement of MIPAS with MLS is better than for daytime and the differences between MIPAS with MLS, GOMOS and SMILES are very similar, and are in the range of 5–10%. The larger differences and their opposite signs in the comparison with SABER have already been discussed above.

At the altitude of the secondary maximum, the agreement between the three instruments for nighttime conditions, is very good, with differences comprised within $\pm 10\%$. MIPAS and SMILES O_3 are very similar, with GOMOS O_3 concentrations being about 10% smaller and SABER about 10% larger. The secondary peak is practically at the same altitude, namely ~ 95 km.

Overall, below 70 km MIPAS O_3 concentrations agree within 5–8% with all comparison instruments except SABER. At these altitudes, MIPAS seems to have a positive bias of 5–8% with respect to MLS, SMILES and GOMOS. The agreement with ACE is better and the differences are within 5% except for a narrow region near 55 km, where ACE is larger by about 10%. SABER seems to have a positive bias in the order of 20–60%, more pronounced during daytime. In the upper mesosphere/lower thermosphere, in the O_3 secondary maximum, the agreement between those instruments is, generally, within $\pm(6$–$10)\%$. Near 80 km, around the O_3 minimum, the nighttime relative differences are larger, within -20% to $+10\%$, and are even larger at daytime but very small in absolute terms (within 0.1 ppmv). In general, the differences between all instruments are mostly within or close to the MIPAS 1σ systematic error margin, except for SABER in the mesosphere, and MLS and ACE near 80 km. The latter discrepancies, however, are caused by the very low O_3 concentrations which explode the relative differences. The fact that the differences sometimes exceed the MIPAS systematic errors (grey shaded area) does not come as a surprise because the systematic error estimates of the comparison instruments are not included.

Compared to the difference with these instruments in the previous version V5R_O3_m22 (López-Puertas et al., 2018), we find that the differences of MIPAS V8R O_3 vmr with respect to MLS, SMILES and GOMOS in the stratosphere are slightly larger (2–3%) than in MIPAS V5R. This is a consequence of the effort of conforming the MIPAS NOM and MA/UA retrievals as much consistent as possible, in particular by using the same spectroscopic database and microwindows. Conversely, the agreement with SABER in this region has been improved. The comparison with MLS at 60–70 km has improved, probably because of the new version of MLS whose retrieval has been extended up to ~ 90 km. The agreement with ACE near the stratopause has also been improved, probably due to improvements in the new version of ACE-FTS data. Further, the agreement of the new version of MIPAS with all instruments has been significantly improved in the upper mesosphere/lower thermosphere, reducing the differences from $\sim \pm 20\%$ to $\sim \pm 10\%$. In this respect, the new O_3 a priori of MIPAS (particularly in the daytime) and the smaller relaxation/quenching of $O_3(v_1,v_3)$ by atomic oxygen are the reasons for the better agreement. In addition, the diurnal variation of O_3 in the upper mesosphere (near 80 km, see Fig. D3) has also been ameliorated.

8   Summary and Conclusions

In this work, we present the most recent version of the MIPAS middle and upper atmosphere ozone data (versions V8R_O3_561, V8R_O3_661 and V8R_O3_761), covering altitudes from 20 up to 100/105 km, retrieved from MIPAS observations in the three middle atmosphere modes MA, UA and NLC. This data version is based in the most recent version 8 level 1b MIPAS spectra, which were processed with a retrieval algorithm that incorporates several improvements over the previous data version (V5R_O3_m22). Among them are: a more accurate retrieved temperature, the treatment of the background continuum and radiance offset correction, and the selection of optimized numerical settings. Microwindows and spectroscopic data were also updated to be consistent with the O_3 retrieval of the nominal (NOM) mode (Kiefer et al., 2023). Specific to

the middle/upper atmospheric O_3 are three important updates: the O_3 a priori data (particularly important for daytime), the revision of the non-LTE processes, and the atomic oxygen concentration during nighttime.

Another different aspect of this version is the novel treatment of errors, following the TUNER (Towards Unified Error Reporting) recommendations (von Clarmann et al., 2022), where the different components (random or systematic) of a given error source were propagated independently and where correlations and compensation effects caused by the propagation of uncertainties in parameters obtained in preceding retrieval steps, such as temperature, were taken into account. The random component of the O_3 error is dominated by the measurement noise. Typical values (1σ for single profiles) for daytime are smaller than 5% below ~60 km, 5–10% between 60 and 70 km, 10–20% at 70–90 km and about 30% at 95 km. For nighttime, they are very similar to those for daytime below 70 km but significantly smaller above, with values of 10–20% at 75–95 km, 20–30% at 95–100 km and larger than 30% above 100 km. The random O_3 error is generally larger than the total systematic uncertainty above around ~60 km.

The systematic error is dominated by the uncertainties of spectroscopic data below ~60 km (~6%), with a significant contribution of the ILS and, to a lesser extent, the persistent part of the gain calibration uncertainty. Above ~60 km the systematic errors are dominated by the non-LTE uncertainties but the spectroscopic data error also contributes significantly under certain conditions. The non-LTE errors are smaller than 1% below 60 km, 2–8% at 60–85 km, and 5–12% above 85 km. The ILS contribution is also appreciable at above ~90 km. As a consequence of the new TUNER method, which takes compensation effects of errors that act via multiple pathways into account, the estimates of systematic errors in the 80–100 km range are significantly smaller than those of version V5R_O3_m22 (see Fig. 5 and Table 4 in López-Puertas et al., 2018). On one hand, non-LTE errors are smaller, because of a proper propagation of the atomic oxygen abundance, but also the O_3 errors incurred by the uncertainties in temperature and in the systematic component of the gain are smaller, as they partially compensate.

When comparing with the previous V5R_O3_m22 version, we note: 1) that O_3 abundance is larger in about 2–5% (0.2–0.5 ppmv) at 20–50 km; 2) a decrease by ~2–4% between 50 and 60 km, mainly in the tropics and mid-latitudes; 3) a more pronounced nighttime O_3 minimum just below 80 km leading to a more realistic diurnal variation in this region; 4) a larger (~40%, 0.2–0.3 ppmv) O_3 concentration in the secondary maximum during daytime in the tropical and mid-latitudes; and 5) a 10–30% decrease in the O_3 abundance in the secondary maximum at nighttime.

We found that the O_3 fields retrieved from the nominal mode (NOM) and the middle atmosphere modes in their common altitude range (20–70 km) are fully consistent, with differences generally being within 1–2%. This is essential for studies involving a combined dataset. Only in the lower mesosphere (60–70 km) during daytime O_3 NOM seems to be larger than O_3 MA/UA in 2–10% for most latitudes.

The comparison performed with the most recent data versions of SABER, GOMOS, MLS, SMILES and ACE-FTS, shows that MIPAS O_3 is within 5% and 8% below 70 km with all instruments except SABER. In this region, MIPAS seems to have a positive bias of 5–8% with respect to MLS, SMILES and GOMOS. The agreement with ACE is better and the differences are within 5% except for a narrow region near 55 km, where ACE is larger by about 10%. SABER seems to have a positive bias in the order of 20–60%, more pronounced during daytime.

In the upper mesosphere/lower thermosphere, the agreement between those instruments is, generally, within ± 6–10%. Near the O_3 minimum around 80 km, the nighttime relative differences are larger (within -20 to $+10\%$), and are larger at daytime, but very small in absolute terms (within 0.1 ppmv).

In general, the differences between all instruments are mostly within or near the 1σ systematic error margin of MIPAS, except for SABER in the mesosphere, and MLS and ACE near 80 km. The latter, however, is due to the very low O_3 abundance.

Comparing these differences with those reported by (López-Puertas et al., 2018) for the previous version V5R_O3_m22 (López-Puertas et al., 2018), we find that the differences with MLS, SMILES and GOMOS are slightly larger (2–3%) in the stratosphere. This is the result of using a different spectroscopic database in this version. Conversely, the agreement with SABER in this region has been improved. The comparison with MLS at 60–70 km has improved, probably because the new version of MLS has been extended up to ~ 90 km. The agreement with ACE near the stratopause has also improved (likely originated by the new version of ACE). Noticeably, the new version of MIPAS agrees much better than before with all instruments in the upper mesosphere/lower thermosphere, reducing the differences from $\sim \pm 20\%$ to $\sim \pm 10\%$. Further, the diurnal variation of O_3 in the upper mesosphere (near 80 km) has been significantly improved.

Data availability. The MIPAS data can be obtained from the KITopen repository. The data will also be available on demand in HAR-MOZ format (Sofieva et al., 2013, https://essd.copernicus.org/articles/5/349/2013/). SABER version 2.0 of O_3 retrieved from the 9.6 μm channel are publicly available at http://saber.gats-inc.com. The ESA O_3 IPF version 6.01 (Kyrölä et al., 2010; Sofieva et al., 2010) are available from the ESA Earth online portal (https://earth.esa.int). MLS O_3 version 5.0-1.1a is available from https://mls.jpl.nasa.gov. SMILES O_3 data version 3.2 is available from http://darts.isas.jaxa.jp/stp/smiles/. ACE-FTS O_3 data from version 4.1. is available from http://www.ace.uwaterloo.ca/data.php.

The supplement related to this article is available online at https://doi.org/10.5194/amt-0-1-2023-supplement.

Author contributions. MLP performed the data analysis, wrote the manuscript and had the final editorial responsibility for this paper. MGC performed the comparison of MIPAS data with all the other instruments. BF developed the retrieval setup and performed many test calculations. TvC ensured the TUNER compliance of error estimates. NG was responsible for spectroscopy issues, developed parts of the error estimation software, and carried out some retrieval tests. UG provided and maintained the retrieval software and developed parts of the error estimation software. SK and ALi ran the retrievals. MK coordinated and performed related test calculations and error estimations. ALa contributed to quality control and prepare the data in HARMOZ format. GPS organized the interfacing between IMK and IAA, the consistency between NOM and MA/UA/NLC data, and took care of the quality control. All the authors participated in the development of the retrieval setup, contributed to the discussions, and provided text and comments.

Competing interests. At least one of the (co-)authors is a member of the editorial board of Atmospheric Measurement Techniques. The peer-review process was guided by an independent editor, and the authors also have no other competing interests to declare.

Acknowledgements. We would like to thank the European Space Agency for providing the MIPAS level 1b spectra. The IAA team acknowledges financial support from the Agencia Estatal de Investigación, MCIN/AEI/10.13039/501100011033, through grants PID2019-

705   110689RB-I00 and CEX2021-001131-S. The Karlsruhe Institute of Technology (KIT) team was supported by the Deutsches Zentrum für Luft- und Raumfahrt (DLR) under contract no. 50EE1547. The computations were partly done in the framework of a Bundesprojekt (grant MIPAS_V7) on the Cray XC40 "Hazel Hen" of the High-Performance Computing Center Stuttgart (HLRS) of the University of Stuttgart.

References

Bernath, P. F.: The Atmospheric Chemistry Experiment (ACE), J. Quant. Spectrosc. Radiat. Transf., 186, 3–16, https://doi.org/10.1016/j.jqsrt.2016.04.006, 2017.

Bertaux, J. L., Kyrölä, E., Fussen, D., Hauchecorne, A., Dalaudier, F., Sofieva, V., Tamminen, J., Vanhellemont, F., Fanton D'Andon, O., Barrot, G., Mangin, A., Blanot, L., Lebrun, J. C., Pérot, K., Fehr, T., Saavedra, L., Leppelmeier, G. W., and Fraisse, R.: Global ozone monitoring by occultation of stars: an overview of GOMOS measurements on ENVISAT, Atmospheric Chemistry & Physics, 10, 12 091–12 148, https://doi.org/10.5194/acp-10-12091-2010, 2010.

Birk, M., Wagner, G., Gordon, I. E., and Drouin, B. J.: Ozone Intensities in the Rotational Bands, Journal of Quantitative Spectroscopy and Radiative Transfer, 226, 60–65, https://doi.org/10.1016/j.jqsrt.2019.01.004, 2019.

Boone, C. D., Walker, K. A., , and Bernath, P. F.: Version 3 retrievals for the Atmospheric Chemistry Experiment Fourier Transform Spectrometer (ACE–FTS), in: The Atmospheric Chemistry Experiment ACE at 10: A Solar Occultation Anthology, edited by Bernath, P. F., pp. 103–127, A. Deepak Publishing, Hampton, Virginia, U.S.A., 2013.

Brasseur, G. and Solomon, S.: Aeronomy of the Middle Atmosphere–Chemistry and Physics of the Stratosphere and Mesosphere, Atmospheric and Oceanographic Sciences Library 32, Springer, P. O. Box 17, 3300 AA Dordrecht, The Netherlands, third edn., 2005.

Castle, K. J., Black, L. A., and Pedersen, T. J.: Vibrational Relaxation of $O_3(\nu_2)$ by $O(^3P)$, The Journal of Physical Chemistry, pp. 1–6, https://doi.org/10.1021/jp500224j, 2014.

De Laurentis, M.: Planning of MIPAS new special modes January 2005 Campaign, Tech. rep., ESA Technical Note, ENVI-SPPA-EOPG-TN-05-0002, 2005.

Eckert, E., von Clarmann, T., Kiefer, M., Stiller, G. P., Lossow, S., Glatthor, N., Degenstein, D., Froidevaux, L., Godin-Beekmann, S., Leblanc, T., McDermid, S., Pastel, M., Steinbrecht, W., Swart, D. P. J., Walker, K. A., and Bernath, P. F.: Drift-Corrected Trends and Periodic Variations in MIPAS IMK/IAA Ozone Measurements, ACP, 14, 2571–2589, https://doi.org/10.5194/acp-14-2571-2014, 2014.

Emmert, J. T., Drob, D. P., Picone, J. M., Siskind, D. E., Jones, M., Mlynczak, M. G., Bernath, P. F., Chu, X., Doornbos, E., Funke, B., Goncharenko, L. P., Hervig, M. E., Schwartz, M. J., Sheese, P. E., Vargas, F., Williams, B. P., and Yuan, T.: NRLMSIS 2.0: A Whole-Atmosphere Empirical Model of Temperature and Neutral Species Densities, Earth Space Sci., 8, https://doi.org/10.1029/2020ea001321, 2021.

Fischer, H., Birk, M., Blom, C., Carli, B., Carlotti, M., von Clarmann, T., Delbouille, L., Dudhia, A., Ehhalt, D., Endemann, M., Flaud, J. M., Gessner, R., Kleinert, A., Koopmann, R., Langen, J., López-Puertas, M., Mosner, P., Nett, H., Oelhaf, H., Perron, G., Remedios, J., Ridolfi, M., Stiller, G., and Zander, R.: MIPAS: an instrument for atmospheric and climate research, Atmos. Chem. Phys., 8, 2151–2188, 2008.

Flaud, J.-M., Piccolo, C., Carli, B., Perrin, A., Coudert, L. H., Teffo, J.-L., and Brown, L. R.: Molecular line parameters for the MIPAS (Michelson Interferometer for Passive Atmospheric Sounding) experiment, Atmos. Oceanic Opt., 16, 172–182, 2003a.

Flaud, J. M., Wagner, G., Birk, M., Camy-Peyret, C., Claveau, C., De Backer-Barilly, M. R., Barbe, A., and Piccolo, C.: Ozone absorption around 10 μm, J. Geophys. Res., 108, 4269, https://doi.org/10.1029/2002JD002755, 2003b.

Funke, B., López-Puertas, M., Stiller, G. P., von Clarmann, T., and Höpfner, M.: A new non–LTE Retrieval Method for Atmospheric Parameters From MIPAS–ENVISAT Emission Spectra, Adv. Space Res., 27, 1099–1104, https://doi.org/10.1016/S0273-1177(01)00169-7, 2001.

Funke, B., López-Puertas, M., García-Comas, M., Kaufmann, M., Höpfner, M., and Stiller, G. P.: GRANADA: a Generic RAdiative traNsfer AnD non-LTE population Algorithm, J. Quant. Spectrosc. Radiat. Transfer, 113, 1771–1817, https://doi.org/10.1016/j.jqsrt.2012.05.001, 2012.

Garcia, R., Smith, A., Kinnison, D., de la Camara, A., and Murphy, D.: Modification of the gravity wave parameterization in the Whole Atmosphere Community Climate Model: Motivation and results, Journal of the Atmospheric Sciences, 74, 275–291, https://doi.org/10.1175/JAS-D-16-0104.1, 2017.

Garcia, R. R. and Solomon, S.: A new numerical model for the middle atmosphere 2. Ozone and related species, J. Geophys. Res., 99, 12 937–12 951, 1994.

García-Comas, M., Funke, B., and al., e.: IMK/IAA MIPAS Temperature Retrieval Version 8: Middle Atmosphere Measurements, Atmospheric Measurement Techniques Discussions, https://doi.org/10.5194/amt-2023, 2023.

Gil-López, S., López-Puertas, M., Kaufmann, M., Funke, B., García-Comas, M., Koukouli, M. E., Glatthor, N., Grabowski, U., Höpfner, Stiller, G. P., and von Clarmann, T.: Retrieval of stratospheric and mesospheric O_3 from high resolution MIPAS spectra at 15 and 10 μm, Adv. Space Res., 36, 943–951, https://doi.org/10.1016/j.asr.2005.05.123, 2005.

Glatthor, N., von Clarmann, T., Fischer, H., Funke, B., Gil-López, S., Grabowski, U., Höpfner, M., Kellmann, S., Linden, A., López-Puertas, M., Mengistu Tsidu, G., Milz, M., Steck, T., Stiller, G. P., and Wang, D.-Y.: Retrieval of stratospheric ozone profiles from MIPAS/ENVISAT limb emission spectra: a sensitivity study, Atmos. Chem. Phys., 6, 2767–2781, 2006.

Glatthor, N., von Clarmann, T., Stiller, G. P., Kiefer, M., Laeng, A., Dinelli, B. M., Wetzel, G., and Orphal, J.: Differences in Ozone Retrieval in MIPAS Channels A and AB: A Spectroscopic Issue, Atmospheric Measurement Techniques, 11, 4707–4723, https://doi.org/10.5194/amt-11-4707-2018, 2018.

Gordon, I. E., Rothman, L. S., Hill, C., Kochanov, R. V., Tan, Y., Bernath, P. F., Birk, M., Boudon, V., Campargue, A., Chance, K. V., Drouin, B. J., Flaud, J. M., Gamache, R. R., Hodges, J. T., Jacquemart, D., Perevalov, V. I., Perrin, A., Shine, K. P., Smith, M. A. H., Tennyson, J., Toon, G. C., Tran, H., Tyuterev, V. G., Barbe, A., Császár, A. G., Devi, V. M., Furtenbacher, T., Harrison, J. J., Hartmann, J. M., Jolly, A., Johnson, T. J., Karman, T., Kleiner, I., Kyuberis, A. A., Loos, J., Lyulin, O. M., Massie, S. T., Mikhailenko, S. N., Moazzen-Ahmadi, N., Müller, H. S. P., Naumenko, O. V., Nikitin, A. V., Polyansky, O. L., Rey, M., Rotger, M., Sharpe, S. W., Sung, K., Starikova, E., Tashkun, S. A., Auwera, J. V., Wagner, G., Wilzewski, J., Wcisło, P., Yu, S., and Zak, E. J.: The HITRAN2016 molecular spectroscopic database, Satellite Remote Sensing and Spectroscopy: Joint ACE-Odin Meeting, October 2015, 203, 3–69, 2017.

Hubert, D., Keppens, A., Granville, J., and Lambert, J.-C.: Multi-TASTE Phase F Validation Report: Ground-based validation of MIPAS ESA operational products (ORM 8.22): T, altitude, O_3, CH_4, HNO_3 and N_2O, available at: https://earth.esa.int/eogateway/documents/20142/37627/TN-BIRA-IASB-MultiTASTE-Phase-F-MIPAS-ORM8-Iss1-RevB.pdf (last access: 10 March 2023), 2020.

Imai, K., Fujiwara, M., Inai, Y., Manago, N., Suzuki, M., Sano, T., Mitsuda, C., Naito, Y., Hasebe, F., Koide, T., and Shiotani, M.: Comparison of ozone profiles between Superconducting Submillimeter-Wave Limb-Emission Sounder and worldwide ozonesonde measurements, J. Geophys. Res., 118, 12,755–12,765, https://doi.org/10.1002/2013JD021094, 2013a.

Imai, K., Manago, N., Mitsuda, C., Naito, Y., Nishimoto, E., Sakazaki, T., Fujiwara, M., Froidevaux, L., von Clarmann, T., Stiller, G. P., Murtagh, D. P., Rong, P.-p., Mlynczak, M. G., Walker, K. A., Kinnison, D. E., Akiyoshi, H., Nakamura, T., Miyasaka, T., Nishibori, T., Mizobuchi, S., Kikuchi, K.-i., Ozeki, H., Takahashi, C., Hayashi, H., Sano, T., Suzuki, M., Takayanagi, M., and Shiotani, M.: Validation of ozone data from the Superconducting Submillimeter-Wave Limb-Emission Sounder (SMILES), J. Geophys. Res., 118, 5750–5769, 2013b.

Jurado-Navarro, A. A., López-Puertas, M., Funke, B., Garcia-Comas, M., Gardini, A., González-Galindo, F., Stiller, G. P., Clarmann, T. V., Grabowski, U., and Linden, A.: Global distributions of CO2 volume mixing ratio in the middle and upper atmosphere from daytime MIPAS high-resolution spectra, Atmospheric Measurement Techniques, 9, 6081–6100, https://doi.org/10.5194/amt-9-6081-2016, 2016.

785 Kaufmann, M., Gusev, O. A., Grossmann, K. U., Martín-Torres, F. J., Marsh, D. R., and Kutepov, A. A.: Satellite observations of daytime and nighttime ozone in the mesosphere and lower thermosphere, J. Geophys. Res., 108, 4399, https://doi.org/10.1029/2002JD003186, 2003.

Kiefer, M., von Clarmann, T., Funke, B., García-Comas, M., Glatthor, N., Grabowski, U., Kellmann, S., Kleinert, A., Laeng, A., Linden, A., López-Puertas, M., Marsh, D. R., and Stiller, G. P.: IMK/IAA MIPAS Temperature Retrieval Version 8: Nominal Measurements, Atmospheric Measurement Techniques, 14, 4111–4138, https://doi.org/10.5194/amt-14-4111-2021, 2021.

790 Kiefer, M., von Clarmann, T., Funke, B., García-Comas, M., Glatthor, N., Grabowski, U., Höpfner, M., Kellmann, S., Laeng, A., Linden, A., López-Puertas, M., and Stiller, G. P.: Version 8 IMK–IAA MIPAS Ozone Profiles: Nominal Observation Mode, Atmospheric Measurement Techniques, 16, 1443–1460, https://doi.org/10.5194/amt-16-1443-2023, 2023.

Kikuchi, K.-I., Nishibori, T., Ochiai, S., Ozeki, H., Irimajiri, Y., Kasai, Y., Koike, M., Manabe, T., Mizukoshi, K., Murayama, Y., Naga-hama, T., Sano, T., Sato, R., Seta, M., Takahashi, C., Takayanagi, M., Masuko, H., Inatani, J., Suzuki, M., and Shiotani, M.: Overview

795 and early results of the Superconducting Submillimeter-Wave Limb-Emission Sounder (SMILES), J. Geophys. Res., 115, D23 306, https://doi.org/10.1029/2010JD014379, 2010.

Kleinert, A., Birk, M., Perron, G., and Wagner, G.: Level 1b Error Budget for MIPAS on ENVISAT, Atmospheric Measurement Techniques, pp. 1–28, https://doi.org/10.5194/amt-2018-185, 2018.

Kyrölä, E., Tamminen, J., Sofieva, V., Bertaux, J. L., Hauchecorne, A., Dalaudier, F., Fussen, D., Vanhellemont, F., Fanton D'Andon, O.,

800 Barrot, G., Guirlet, M., Mangin, A., Blanot, L., Fehr, T., Saavedra de Miguel, L., and Fraisse, R.: Retrieval of atmospheric parameters from GOMOS data, Atmospheric Chemistry & Physics, 10, 11 881–11 903, https://doi.org/10.5194/acp-10-11881-2010, 2010.

Laeng, A., Grabowski, U., von Clarmann, T., Stiller, G., Glatthor, N., Höpfner, M., Kellmann, S., Kiefer, M., Linden, A., Lossow, S., Sofieva, V., Petropavlovskikh, I., Hubert, D., Bathgate, T., Bernath, P., Boone, C. D., Clerbaux, C., Coheur, P., Damadeo, R., Degenstein, D., Frith, S., Froideveaux, L., Gille, J., Hoppel, J., McHugh, M., Kasai, Y., Lumpe, J., Rahpoe, N., Toon, G., Sano, T., Suzuki, M., Tamminen, J.,

805 Urban, J., Walker, K., Weber, M., and Zawodny, J.: Validation of MIPAS IMK/IAA V5R_O3_224 ozone profiles, Atmos. Meas. Tech., 7, 3971–3987, https://doi.org/10.5194/amt-7-3971-2014, 2014.

Laeng, A., Hubert, D., Verhoelst, T., von Clarmann, T., Dinelli, B. M., Dudhia, A., Raspollini, P., Stiller, G., Grabowski, U., Keppens, A., Kiefer, M., Sofieva, V., Froidevaux, L., Walker, K. A., Lambert, J.-C., and Zehner, C.: The Ozone Climate Change Initiative: Comparison of four Level-2 Processors for the Michelson Interferometer for Passive Atmospheric Sounding (MIPAS), Remote Sens. Environ., 162,

810 316–343, https://doi.org/10.1016/j.rse.2014.12.013, 2015.

Laeng, A., Eckert, E., von Clarmann, T., Kiefer, M., Hubert, D., Stiller, G., Glatthor, N., López-Puertas, M., Funke, B., Grabowski, U., Plieninger, J., Kellmann, S., Linden, A., Lossow, S., Babenhauserheide, A., Froidevaux, L., and Walker, K.: On the improved stability of the version 7 MIPAS ozone record, Atmos. Meas. Tech., 11, 4693–4705, https://doi.org/10.5194/amt-11-4693-2018, 2018.

Livesey, N. J., Read, W. G., Wagner, P. A., Froidevaux, L., Santee, M. L., Schwartz, M. J., Lambert, A., Millán-Valle, L. F., Pumphrey,

815 H. C., , Manney, G. L., Fuller, R. A., Jarnot, R. F., Knosp, B. W., and Lay, R. R.: Version 5.0x Level 2 and 3 data quality and description document, Tech. Rep. JPL D-105336 Rev. B, Jet Propulsion Lab, 2022.

López-Puertas, M., Funke, B., Stiller, G., and Laeng, A.: The diurnal variability of O_3 in the upper stratosphere and mesosphere (WP232 and O-WP310), Tech. Rep. Project: Ozone CCI O-II Optional Proposal v1.1, ESA Contract No:4000109876/14/I-NB, European Space Agency, 2017.

820 López-Puertas, M., García-Comas, M., Funke, B., Gardini, A., Stiller, G. P., von Clarmann, T., Glatthor, N., Laeng, A., Kaufmann, M., Sofieva, V. F., Froidevaux, L., Walker, K. A., and Shiotani, M.: MIPAS Observations of Ozone in the Middle Atmosphere, Atmospheric Measurement Techniques, 11, 2187–2212, https://doi.org/10.5194/amt-11-2187-2018, 2018.

Marsh, D. R.: Chemical-Dynamical Coupling in the Mesosphere and Lower Thermosphere, in: Aeronomy of the Earth's Atmosphere and Ionosphere, vol. 2, pp. 3–17, Springer, Dordrecht, iaga special sopron book edn., 2011.

825 Marsh, D. R., Mills, M. J., Kinnison, D. E., Lamarque, J.-F., Calvo, N., and Polvani, L. M.: Climate Change from 1850 to 2005 Simulated in CESM1(WACCM), Journal of Climate, 26, 7372–7391, https://doi.org/10.1175/JCLI-D-12-00558.1, 2013.

Mitsuda, C., Suzuki, M., Iwata, Y., Manago, N., Naito, Y., Takahashi, C., Imai, K., Nishimoto, E., Hayashi, H., Shiotani, M., Sano, T., Takayanagi, M., and Taniguchi, H.: Current status of level 2 product of Superconducting Submillimeter-Wave Limb-Emission Sounder (SMILES), in: Sensors, Systems, and Next-Generation Satellites XV edited by Roland Meynart, Steven P. Neeck, Haruhisa Shimoda,

830 edited by Meynart, R., Neeck, S. P., and Shimoda, H., vol. 8176, p. 6, SPIE, https://doi.org/10.1117/12.898135, 2011.

Mlynczak, M. G., Hunt, L. A., Mast, J. C., Thomas Marshall, B., Russell, J. M., Smith, A. K., Siskind, D. E., Yee, J.-H., Mertens, C. J., Javier Martin-Torres, F., Earl Thompson, R., Drob, D. P., and Gordley, L. L.: Atomic oxygen in the mesosphere and lower thermosphere derived from SABER: Algorithm theoretical basis and measurement uncertainty, J. Geophys. Res., 118, 5724–5735, https://doi.org/10.1002/jgrd.50401, 2013.

835 Norton, H. and Beer, R.: New apodizing functions for Fourier spectrometry, J. Opt. Soc. Am., 66, 259–264, (Errata J. Opt. Soc. Am., 67, 419,1977), 1976.

Oelhaf, H.: MIPAS Mission Plan, ESA Technical Note ENVI-SPPA-EOPG-TN-07-0073, 2008.

Picone, J., Hedin, A., Drob, D., and Aikin, A.: NRLMSISE-00 empirical model of the atmosphere: Statistical comparisons and scientific issues, J. Geophys. Res., 107, 1468, doi:10.1029/2002JA009 430, 2002.

840 Rong, P. P., Russell, J. M., Mlynczak, M. G., Remsberg, E. E., Marshall, B. T., Gordley, L. L., and López-Puertas, M.: Validation of Thermosphere Ionosphere Mesosphere Energetics and Dynamics/Sounding of the Atmosphere using Broadband Emission Radiometry (TIMED/SABER) v1.07 ozone at 9.6 μm in altitude range 15-70 km, J. Geophys. Res., 114, D04 306, https://doi.org/10.1029/2008JD010073, 2009.

Rothman, L. S., Gordon, I. E., Barbe, A., Benner, D. C., Bernath, P. F., Birk, M., Boudon, V., Brown, L. R., Campargue, A., Champion,

845 J., Chance, K., Coudert, L. H., Dana, V., Devi, V. M., Fally, S., Flaud, J., Gamache, R. R., Goldman, A., Jacquemart, D., Kleiner, I., Lacome, N., Lafferty, W. J., Mandin, J., Massie, S. T., Mikhailenko, S. N., Miller, C. E., Moazzen-Ahmadi, N., Naumenko, O. V., Nikitin, A. V., Orphal, J., Perevalov, V. I., Perrin, A., Predoi-Cross, A., Rinsland, C. P., Rotger, M., $v_S$ime$v_c$ková, M., Smith, M. A. H., Sung, K., Tashkun, S. A., Tennyson, J., Toth, R. A., Vandaele, A. C., and Vander Auwera, J.: The HITRAN 2008 molecular spectroscopic database, J. Quant. Spectrosc. Radiat. Transfer, 110, 533–572, https://doi.org/10.1016/j.jqsrt.2009.02.013, 2009.

850 Russell III, J. M., Mlynczak, M. G., Gordley, L. L., Tansock, J., and Esplin, R.: An overview of the SABER experiment and preliminary calibration results, in: Optical Spectroscopic Techniques and Instrumentation for Atmospheric and Space Research III, edited by Larar, A. M., vol. 3756, pp. 277–288, 1999.

Schwartz, M., Froidevaux, L., Livesey, N., and Read, W.: MLS/Aura Level 2 Ozone (O3) Mixing Ratio V004, in: Accessed October 2017, Goddard Earth Sciences Data and Information Services Center (GES DISC), https://doi.org/doi: 10.5067/AURA/MLS/DATA2017, 2015.

855 Smith, A. K., Harvey, V. L., Mlynczak, M. G., Funke, B., García-Comas, M., Hervig, M., Kaufmann, M., Kyrölä, E., López-Puertas, M., McDade, I., Randall, C. E., Russell, J. M., Sheese, P. E., Shiotani, M., Skinner, W. R., Suzuki, M., and Walker, K. A.: Satellite observations of ozone in the upper mesosphere, J. Geophys. Res., 118, 1–19, https://doi.org/10.1002/jgrd.50445, 2013.

Sofieva, V. F., Vira, J., Kyrölä, E., Tamminen, J., Kan, V., Dalaudier, F., Hauchecorne, A., Bertaux, J.-L., Fussen, D., Vanhellemont, F., Barrot, G., and Fanton D'Andon, O.: Retrievals from GOMOS stellar occultation measurements using characterization of modeling errors, Atmospheric Measurement Techniques, 3, 1019–1027, 2010.

Sofieva, V. F., Rahpoe, N., Tamminen, J., Kyrölä, E., Kalakoski, N., Weber, M., Rozanov, A., von Savigny, C., Laeng, A., von Clarmann, T., Stiller, G. P., Lossow, S., Degenstein, D., Bourassa, A., Adams, C., Roth, C., Lloyd, N., Bernath, P., Hargreaves, R. J., Urban, J., Murtagh, D., Hauchecorne, A., Dalaudier, F., van Roozendael, M., Kalb, N., and Zehner, C.: Harmonized dataset of ozone profiles from satellite limb and occultation measurements, Earth System Science Data, 5, 349–363, 2013.

Takahashi, C., Ochiai, S., and Suzuki, M.: Operational retrieval algorithms for JEM/SMILES level 2 data processing system, Satellite Remote Sensing and Spectroscopy: Joint ACE-Odin Meeting, October 2015, 111, 160–173, 2010.

Takahashi, C., Suzuki, M., Mitsuda, C., Ochiai, S., Manago, N., Hayashi, H., Iwata, Y., Imai, K., Sano, T., Takayanagi, M., and Shiotani, M.: Capability for ozone high-precision retrieval on JEM/SMILES observation, Advances in Space Research, 48, 1076–1085, 2011.

Tamminen, J., Kyrölä, E., Sofieva, V. F., Laine, M., Bertaux, J.-L., Hauchecorne, A., Dalaudier, F., Fussen, D., Vanhellemont, F., Fanton-D'Andon, O., Barrot, G., Mangin, A., Guirlet, M., Blanot, L., Fehr, T., Saavedra de Miguel, L., and Fraisse, R.: GOMOS data characterisation and error estimation, Atmospheric Chemistry & Physics, 10, 9505–9519, https://doi.org/10.5194/acp-10-9505-2010, 2010.

Tikhonov, A.: On the solution of incorrectly stated problems and method of regularization, Dokl. Akad. Nauk. SSSR, 151, 501–504, 1963.

von Clarmann, T., Glatthor, N., Grabowski, U., Höpfner, M., Kellmann, S., Kiefer, M., Linden, A., Mengistu Tsidu, G., Milz, M., Steck, T., Stiller, G. P., Wang, D. Y., Fischer, H., Funke, B., Gil-López, S., and López-Puertas, M.: Retrieval of temperature and tangent altitude pointing from limb emission spectra recorded from space by the Michelson Interferometer for Passive Atmospheric Sounding (MIPAS), J. Geophys. Res., 108, 4736, https://doi.org/10.1029/2003JD003602, 2003.

von Clarmann, T., Höpfner, M., Kellmann, S., Linden, A., Chauhan, S., Grabowski, U., Funke, B., Glatthor, N., Kiefer, M., Schieferdecker, T., , and Stiller, G. P.: Retrieval of temperature H$_2$O, O$_3$, HNO$_3$, CH$_4$, N$_2$O and ClONO$_2$ from MIPAS reduced resolution nominal mode limb emission measurements, Atmos. Meas. Tech., 2, 159–175, 2009.

von Clarmann, T., Glatthor, N., Grabowski, U., Funke, B., Kiefer, M., and Stiller, G. P.: TUNER-compliant error estimation for MIPAS, in preparation for submission to Atmos. Meas. Tech., 2022.

Waters, J. W., Froidevaux, L., Harwood, R. S., Jarnot, R. F., Pickett, H. M., Read, W. G., Siegel, P. H., Cofield, R. E., Filipiak, M. J., Flower, D. A., Holden, J. R., Lau, G. K., Livesey, N. J., Manney, G. L., Pumphrey, H. C., Santee, M. L., Wu, D. L., Cuddy, D. T., Lay, R. R., Loo, M. S., Perun, V. S., Schwartz, M. J., Stek, P. C., Thurstans, R. P., Boyles, M. A., Chandra, K. M., Chavez, M. C., Chen, G.-S., Chudasama, B. V., Dodge, R., Fuller, R. A., Girard, M. A., Jiang, J. H., Jiang, Y., Knosp, B. W., Labelle, R. C., Lam, J. C., Lee, A. K., Miller, D., Oswald, J. E., Patel, N. C., Pukala, D. M., Quintero, O., Scaff, D. M., Vansnyder, W., Tope, M. C., Wagner, P. A., and Walch, M. J.: The Earth Observing System Microwave Limb Sounder (EOS MLS) on the Aura Satellite, IEEE Transactions on Geoscience and Remote Sensing, 44, 1075–1092, https://doi.org/10.1109/TGRS.2006.873771, 2006.

West, G. A., Weston Jr., R. E., and Flynn, G. W.: Deactivation of vibrationally excited ozone by O(^{3}P) atoms, Chem. Phys. Lett., 42, 488–493, 1976.

West, G. A., Weston, R. E., and Flynn, G. W.: The influence of reactant vibrational excitation on the O(^3P)+O$_3$ bimolecular reaction rate, Chem. Phys. Lett., 56, 429–433, 1978.

Appendix A: Microwindows

Table A1 lists the microwindows and altitude ranges used in the retrieval of MIPAS ozone V8R_O3_m61.

Table A1. Microwindows and altitude ranges used in the retrieval of MIPAS ozone V8R_O3_m61. Microwindows #1–30 falls within band A (685–980 cm^{-1}) of MIPAS and microwindows #31–38 within band AB (1010–1180 cm^{-1}).

No.	Wavenumber (cm^{-1}) Minimum	Maximum
1	687.6875	688.6875
2	689.3125	691.8750
3	692.2500	695.1875
4	707.1250	710.0625
5	712.3125	713.4375
6	713.5000	716.4375
7	716.5000	719.4375
9	728.5000	729.3750
10	730.0625	730.5000
11	731.9375	732.8750
12	734.0000	734.7500
13	736.4375	739.3750
14	739.4375	741.9375
15	745.2500	745.6875
16	746.6875	747.1250
17	747.6250	748.3750
18	749.5625	752.5000
19	752.9375	755.8750
20	758.3750	759.4375
21	759.5000	761.8750
22	765.0000	765.6250
23	767.5000	768.0000
24	771.8750	772.1250
25	774.2500	774.5625
26	776.5000	776.7500
27	780.2500	781.9375
28	788.9375	789.6875
29	790.7500	791.0000
30	791.1875	791.5625
31	1034.1250	1034.3750
32	1034.4375	1035.0000
33	1038.1875	1039.0000
34	1040.0000	1040.8125
35	1048.8125	1049.5000
36	1050.6250	1051.8125
37	1053.3125	1053.7500
38	1054.6875	1055.4375

895 Appendix B: Tables of the O$_3$ error budget

In this section we include tables of the O$_3$ error budget for the atmospheric conditions at selected altitudes discussed in Secs. 4.2.1 and 4.2.2.

Table B1. Ozone error budget for Tropics day, MA. All uncertainties are 1σ.

altitude (km)	mean O_3 vmr (ppmv)	NLTE (%)	interf (%)	ILS (%)	offset (%)	gain (%)	spectro (%)	T+LOS (%)	noise (%)	random (%)	syst (%)
20	1.0	<0.1	1.9	1.8	1.1	0.4	9.1	1.9	3.6	4.8	9.2
30	11	<0.1	0.1	2.3	0.3	1.8	6.8	0.7	1.0	1.4	7.4
40	6.6	<0.1	0.2	2.0	0.3	1.6	6.9	0.7	1.3	1.7	7.3
50	2.6	<0.1	0.1	2.4	0.4	0.5	5.2	0.6	2.2	2.4	5.8
60	1.1	0.2	<0.1	1.8	1.6	0.8	5.6	2.2	6.3	7.0	5.8
70	0.2	5.1	<0.1	0.4	1.2	0.9	6.4	2.5	12	12	8.1
80	0.2	6.1	<0.1	0.6	2.3	1.2	3.4	0.1	16	16	6.8
90	1.0	6.7	<0.1	2.2	4.8	1.0	3.3	1.3	19	20	7.0
96	0.7	11	<0.1	3.6	9.2	0.9	3.9	1.7	33	35	9.1
100	0.7	10	<0.1	3.5	10	0.7	3.4	1.6	37	38	10

Table B2. Ozone error budget for Tropics night, MA. All uncertainties are 1σ.

altitude (km)	mean O_3 vmr (ppmv)	NLTE (%)	interf (%)	ILS (%)	offset (%)	gain (%)	spectro (%)	T+LOS (%)	noise (%)	random (%)	syst (%)
20	1.0	<0.1	1.7	1.7	1.0	0.4	8.7	1.8	3.6	4.7	8.8
30	11	<0.1	0.1	2.2	0.3	1.8	6.7	0.7	0.9	1.3	7.3
40	6.7	<0.1	0.2	2.0	0.3	1.6	7.0	0.7	1.4	1.8	7.4
50	2.8	<0.1	0.1	2.4	0.4	0.9	5.0	0.6	2.4	2.6	5.5
60	1.5	0.2	<0.1	1.6	1.6	1.0	4.3	2.2	5.3	6.0	4.6
70	1.1	5.2	<0.1	1.6	2.4	1.3	4.8	5.0	9.3	11	7.0
80	0.5	5.9	<0.1	0.6	1.3	2.1	3.6	<0.1	13	14	6.8
90	8.9	7.5	<0.1	0.9	2.6	1.6	2.8	2.1	11	12	7.9
96	14	11	<0.1	0.8	2.8	1.1	2.6	2.7	12	13	11
100	11	10	<0.1	1.9	4.3	0.7	2.8	2.2	17	18	9.3

Table B3. Ozone error budget for Northern midlatitude spring day, MA. All uncertainties are 1σ.

altitude (km)	mean O_3 vmr (ppmv)	NLTE (%)	interf (%)	ILS (%)	offset (%)	gain (%)	spectro (%)	T+LOS (%)	noise (%)	random (%)	syst (%)
20	2.9	<0.1	1.9	0.8	1.0	1.9	4.0	1.4	1.9	3.7	4.1
30	8.1	<0.1	0.2	2.4	0.3	1.7	6.7	0.6	1.1	1.7	7.3
40	6.8	<0.1	0.2	2.1	0.3	1.6	7.1	0.7	1.4	1.8	7.6
50	2.5	<0.1	0.1	2.4	0.4	0.5	5.4	0.6	2.3	2.6	5.9
60	1.0	0.2	<0.1	2.0	1.7	1.1	5.3	2.2	6.1	6.8	5.7
70	0.2	4.1	<0.1	0.5	1.7	1.1	5.3	2.3	11	11	6.5
80	0.2	5.9	<0.1	0.7	2.2	0.9	3.6	0.2	15	15	6.8
90	0.7	5.6	<0.1	2.7	6.4	1.0	3.3	1.5	23	24	6.3
96	0.3	6.1	<0.1	3.9	10	0.7	3.2	1.9	36	37	7.3

Table B4. Ozone error budget for Northern midlatitude spring night, MA. All uncertainties are 1σ.

altitude (km)	mean O_3 vmr (ppmv)	NLTE (%)	interf (%)	ILS (%)	offset (%)	gain (%)	spectro (%)	T+LOS (%)	noise (%)	random (%)	syst (%)
20	2.9	<0.1	1.8	0.8	1.0	1.9	4.1	1.4	1.9	3.7	4.2
30	7.7	<0.1	0.2	2.4	0.3	1.7	6.9	0.7	1.1	1.6	7.5
40	7.0	<0.1	0.2	2.3	0.3	1.5	7.4	0.8	1.5	1.9	7.8
50	2.7	<0.1	0.1	2.4	0.5	1.0	5.1	0.6	2.5	2.7	5.7
60	1.4	0.4	<0.1	1.7	1.6	1.4	3.9	2.2	4.8	5.6	4.4
70	1.1	2.3	<0.1	1.6	2.8	1.6	4.2	4.1	7.8	10	4.9
80	0.2	4.6	<0.1	0.8	1.3	0.9	3.2	<0.1	14	15	5.3
90	7.2	4.4	<0.1	1.0	2.2	1.6	2.9	3.4	11	12	5.1
96	12	6.9	<0.1	1.4	3.0	1.2	2.7	3.8	12	14	6.9
100	7.3	6.7	<0.1	3.1	5.4	1.2	2.8	2.7	21	22	7.1

Table B5. Ozone error budget for Northern polar summer day, MA. All uncertainties are 1σ.

altitude (km)	mean O_3 vmr (ppmv)	NLTE (%)	interf (%)	ILS (%)	offset (%)	gain (%)	spectro (%)	T+LOS (%)	noise (%)	random (%)	syst (%)
20	2.3	<0.1	1.8	1.5	1.0	2.4	4.0	1.4	2.2	3.5	4.8
30	4.6	<0.1	0.1	2.4	0.3	1.8	5.9	0.4	1.0	1.5	6.5
40	6.0	<0.1	<0.1	1.7	0.3	1.7	5.8	0.6	1.4	1.6	6.3
50	2.4	<0.1	0.2	2.5	0.5	1.6	4.5	0.6	2.3	2.5	5.4
60	1.1	0.2	<0.1	1.3	1.2	1.5	4.6	1.7	3.3	4.1	4.9
70	0.4	4.1	<0.1	1.6	2.3	0.9	6.0	2.1	8.6	9.3	7.3
80	0.1	7.6	<0.1	0.8	2.4	0.7	4.0	1.4	15	16	7.9
90	0.9	6.8	<0.1	1.3	4.8	1.2	3.2	4.6	17	19	6.3
96	0.5	11	<0.1	2.8	8.3	1.5	4.2	4.6	31	33	10

Table B6. Ozone error budget for Southern polar winter night, MA. All uncertainties are 1σ.

altitude (km)	mean O_3 vmr (ppmv)	NLTE (%)	interf (%)	ILS (%)	offset (%)	gain (%)	spectro (%)	T+LOS (%)	noise (%)	random (%)	syst (%)
20	2.5	<0.1	1.2	1.9	0.9	2.0	4.7	1.7	1.9	4.1	4.7
30	5.3	<0.1	0.2	2.7	0.4	1.5	6.8	0.8	1.3	1.9	7.4
40	4.4	<0.1	<0.1	3.1	0.3	0.9	6.5	0.7	1.6	2.7	7.0
50	1.8	0.2	0.2	2.2	0.8	1.9	4.8	0.8	3.5	4.0	5.4
60	1.3	0.8	<0.1	1.9	1.4	2.3	3.6	1.8	5.3	6.0	4.5
70	1.3	4.7	<0.1	1.1	2.4	1.7	3.7	5.9	8.8	11	5.4
80	0.6	4.9	<0.1	0.6	1.0	1.9	3.3	1.2	12	13	5.2
90	7.2	6.0	<0.1	1.9	1.9	1.3	2.9	1.0	11	11	6.5
96	6.3	5.6	<0.1	3.6	3.6	1.2	2.7	1.8	15	16	6.4
100	3.6	5.4	<0.1	5.3	6.7	1.2	2.7	2.2	27	28	7.2

Appendix C: Random and systematic components of the O_3 errors

900 We show in this section the random and systematic components of the different error sources shown in Fig. 5 and discussed in Secs. 4.2.1 and 4.2.2.
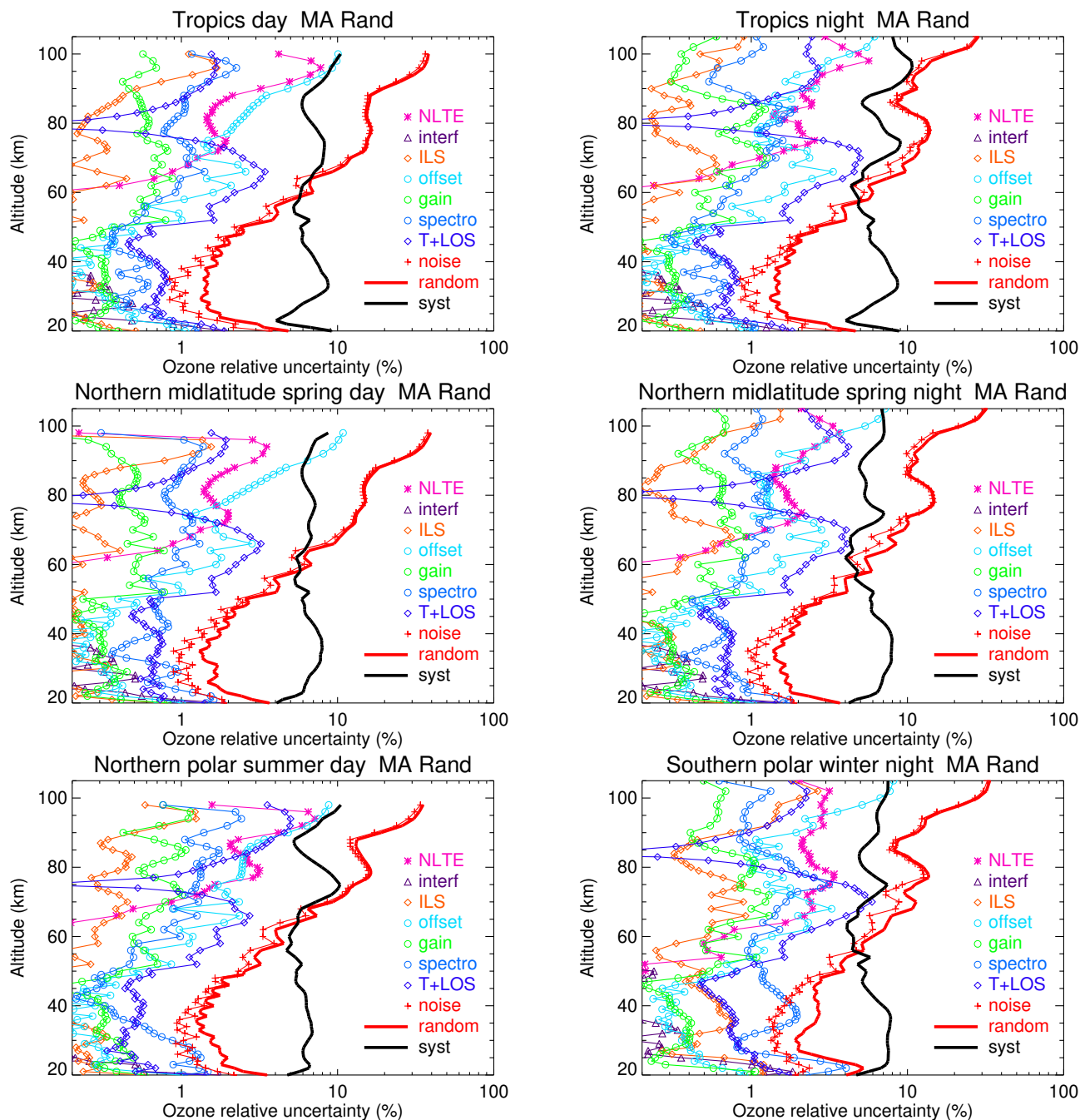
Figure C1. The random components of the O$_3$ error budget for MA data shown in Fig. 5 for different atmospheric conditions (top to bottom) tropics, northern mid-latitudes in spring and polar regions, for daytime (left column) and nighttime (right column). All error estimates are 1-σ uncertainties and given in percentage. Error contributions are labelled "T+LOS" for the propagated error from the T+LOS retrieval, "noise" for error due to measurement noise, "spectro" for the spectroscopic error, "gain" for gain calibration error (see text), "offset" for error due to spectral offset (see text), "ILS" for instrument line shape error (see text), "interf" for the uncertainty in the abundance of the interfering species, and "NLTE" for non-LTE related errors. The total random ("random") and systematic ("syst") errors are also shown.
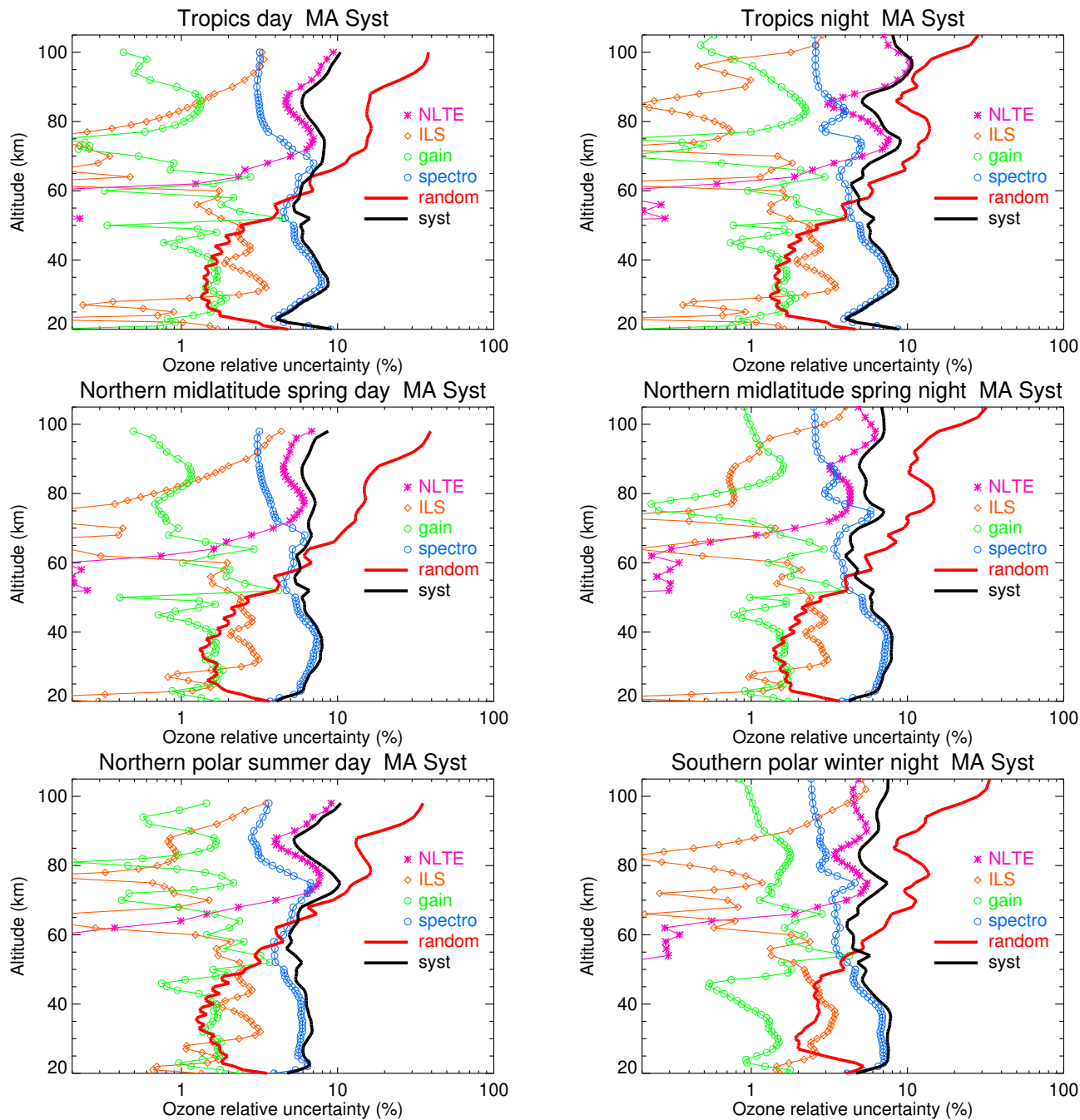
Figure C2. As Fig. C1 but for the systematic components of the O$_3$ errors. The total random ("random") and systematic ("syst") errors are also shown.

Appendix D: O_3 Climatology

We present in this Appendix several distributions of O_3, represented as function of altitude, latitude and time, for the new data version, V8R_O3_m61. Similar figures, and the corresponding discussion of the major features in the O_3 distributions, were presented by López-Puertas et al. (2018) for the previous version, V5R_O3_m22 of MIPAS O_3. The features shown in these figures are very similar. Only the absolute values have changed slightly as have been discussed above in Sec. 5. One significant improvement, however, is the diurnal variation (see Fig. D3). We refer the reader to López-Puertas et al. (2018) for a detailed description of the O_3 fields but recommend to use and cite this new version of MIPAS MA/UA data.

D1 Monthly zonal mean distributions

Figures D1 and D2 show composite monthly zonal means of MIPAS O_3 data for the 2007-2012 period for day- and night-time, respectively. The figures show the characteristic primary, secondary and tertiary maxima and their seasonal evolution (see more details in López-Puertas et al., 2018).

D2 Diurnal variation

For completeness, we also show the composite seasonal zonal mean of the MIPAS O_3 diurnal differences (10 am–10 pm in percentage of 10 pm) in Fig. D3. The differences near 80 km have been considerably improved in the data version. See general features in López-Puertas et al. (2018).

D3 Annual variability

Figure D4 shows the annual variability as latitude$\times$ months cross sections of O_3 at different altitudes for daytime (left column) and nighttime (right column). See López-Puertas et al. (2018) for a description of the major features.

D4 Altitude-resolved time series

In this section we show the inter-annual variability of altitude-resolved time series of O_3 at the tropical and polar latitudes (Fig. D5); and as latitude$\times$time cross sections at given altitudes (Fig. D6).
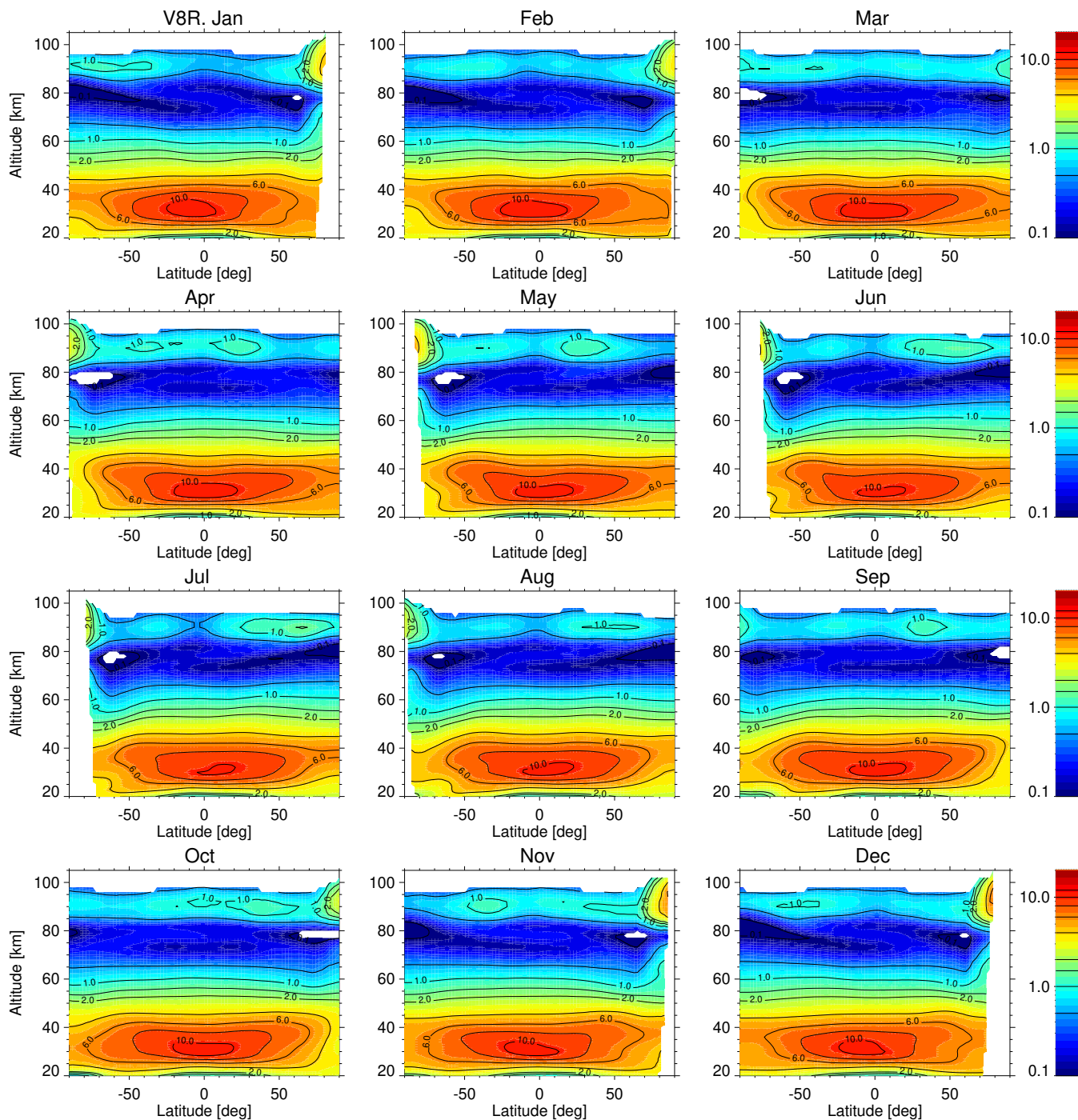
Figure D1. Composite monthly zonal mean of MIPAS data taken in the MA mode for the 2007-2012 period for daytime (local time of 10 am). White areas denote regions where MIPAS has no sensitivity to measure the very low ozone values. Contours are 0.1, 0.5, 1, 1.5, 2, 4, 6, 8, 10 and 12 ppmv.
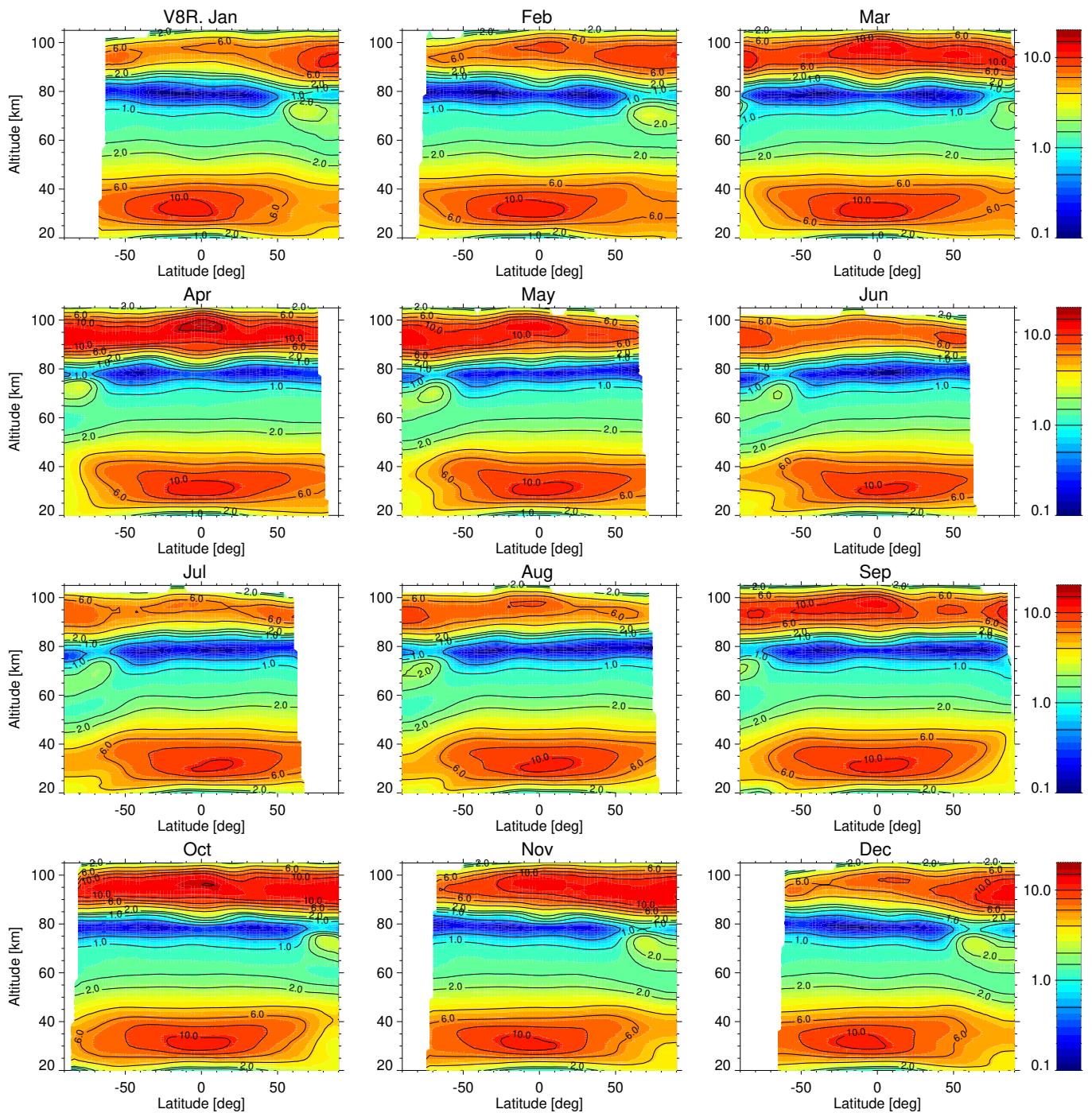
Figure D2. Composite monthly zonal mean of MIPAS data for the 2017-2012 period for nighttime. Contours are 0.5, 1, 1.5, 2, 4, 6, 8, 10, and 15 ppmv.
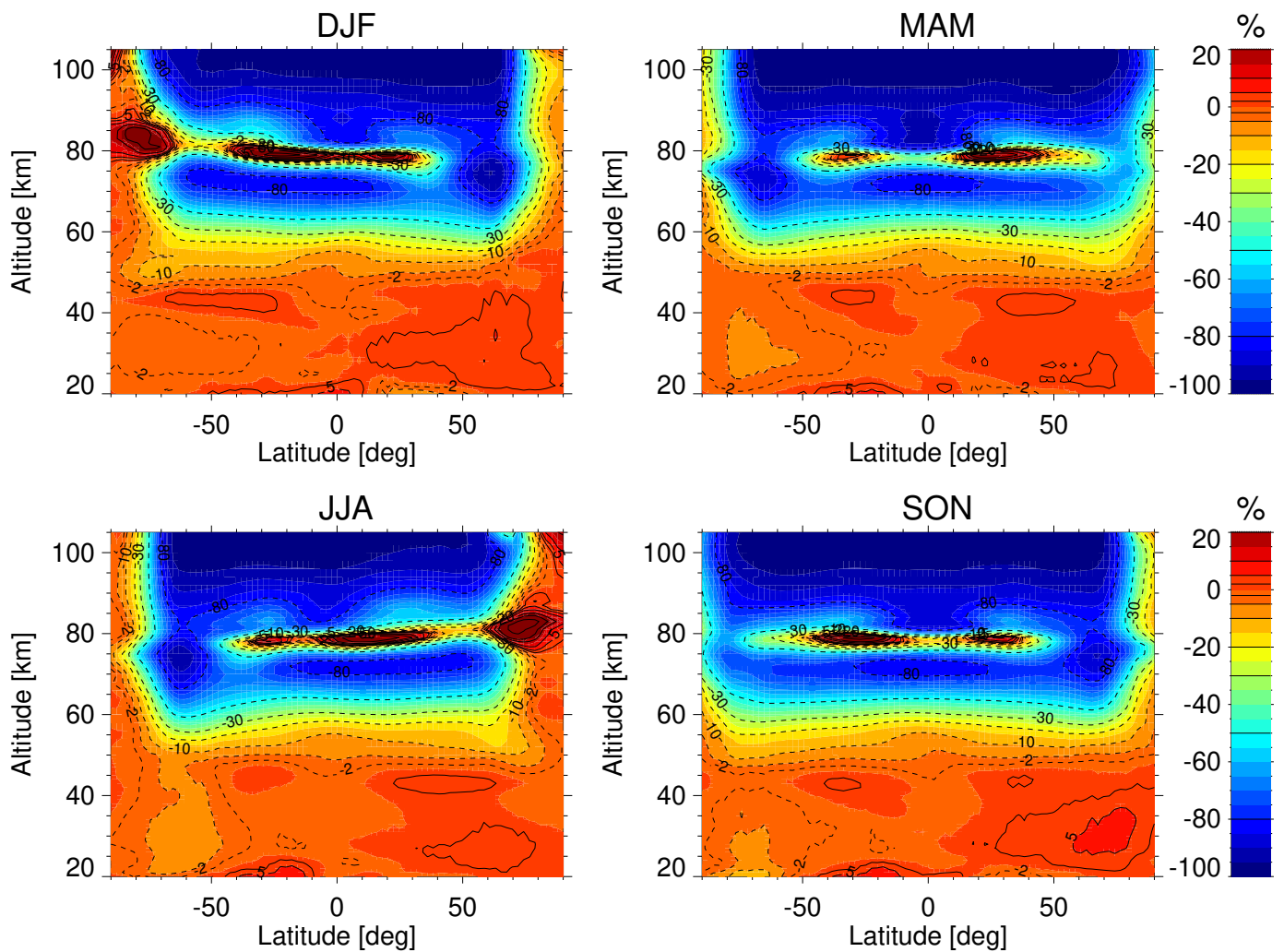
Figure D3. Composite seasonal zonal mean of O_3 diurnal differences (10 am–10 pm in percentage of 10 pm) of MIPAS data taken in the MA mode for the 2007-2012 period. DJF stands for December, January and February; MAM for March, April and May; JJA for June, July and August; and SON for September, October and November. Contours are -80, -50, -30, -20, -10, -5, -2, 2, 5, 10 and 20%.
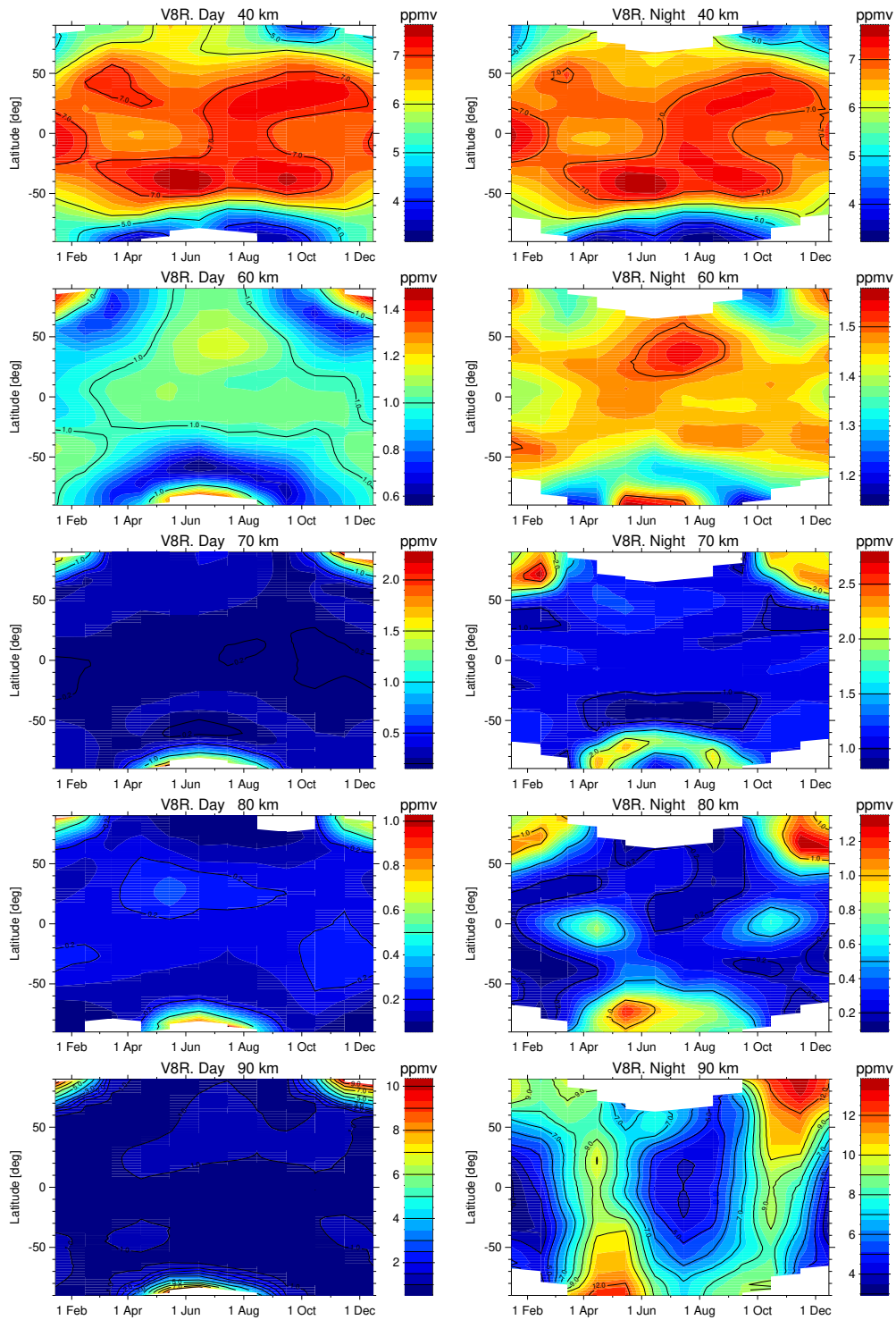
Figure D4. Seasonal evolution versus latitude of O_3 vmr at different altitudes for daytime (left row) and nighttime (right row). Note the different scales used in the different panels.
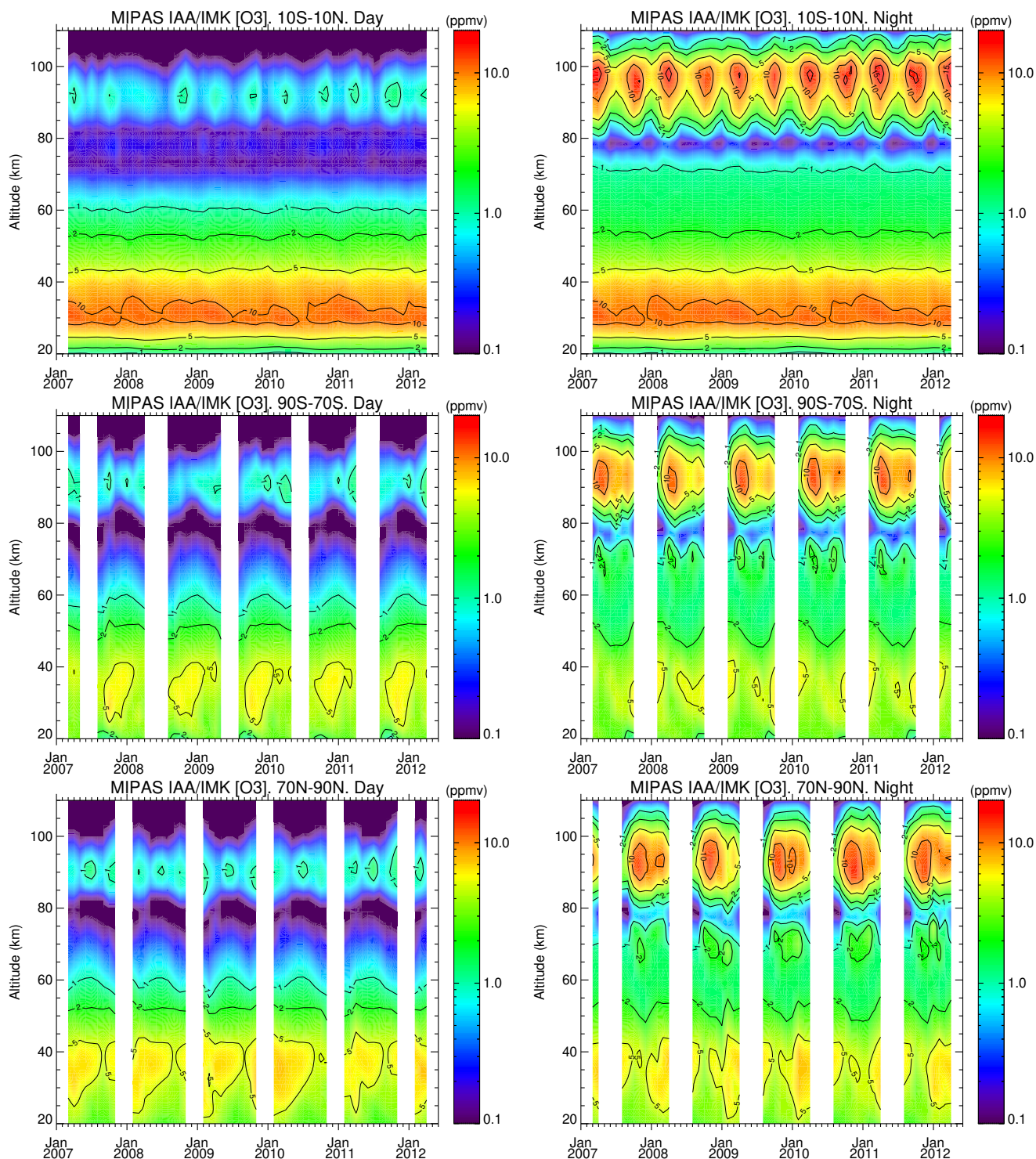
Figure D5. Altitude-resolved time series, for latitudes near the equator (10°S-10°N) (top), the Southern polar region, 70°S-90°S, (middle) and the Northern polar region, 70°N-90°N (bottom), for daytime (left column) and nighttime (right column).
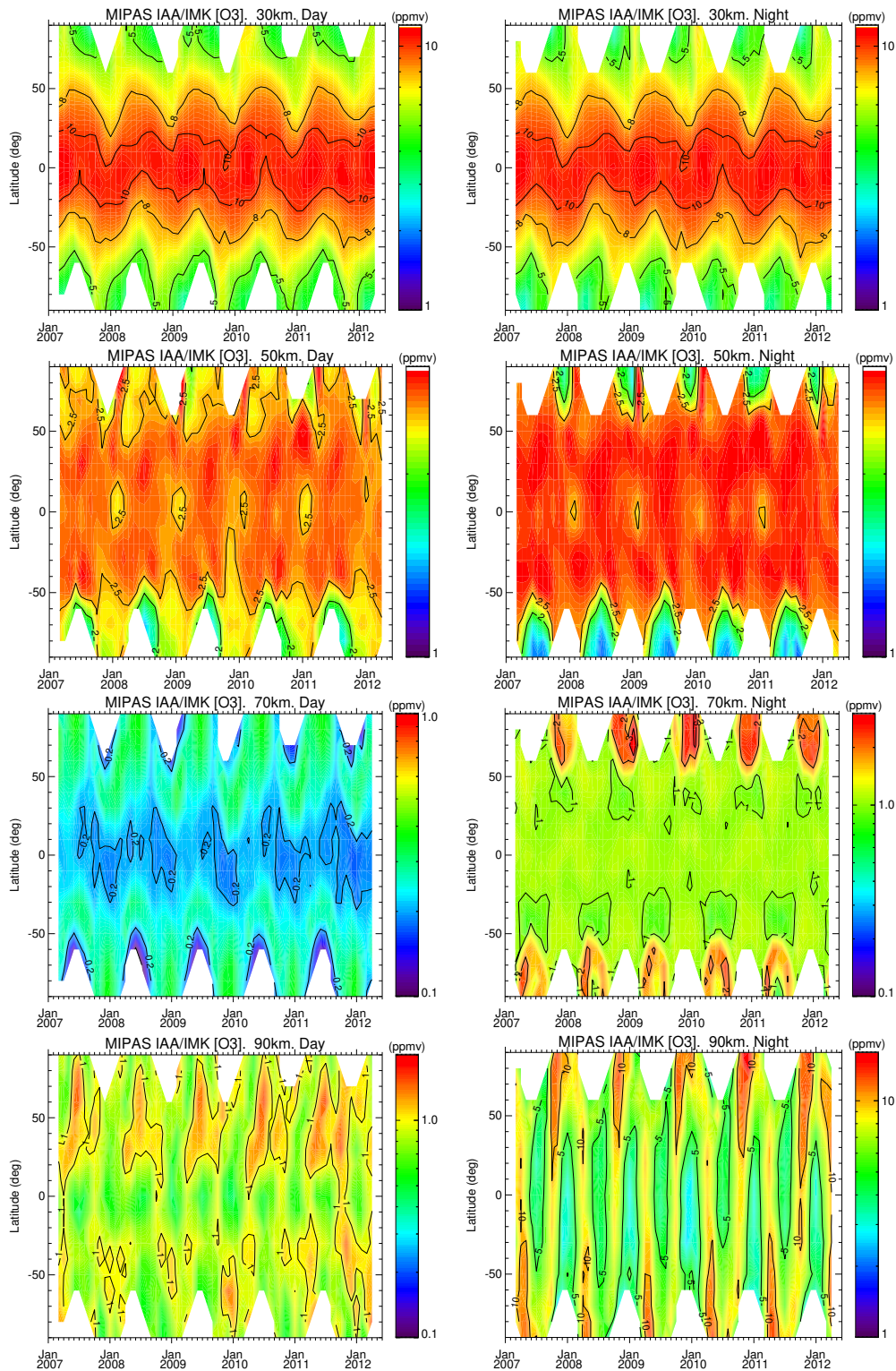
Figure D6. Cross section of latitude/time MIPAS O$_3$ at 50 km, 70 km and 90 km for daytime (left column) and nighttime (right column). Note the different color scales in some panels.